

How alkaline compounds control atmospheric aerosol particle acidity

Vlassis A. Karydis^{1,2*}, Alexandra P. Tsimpidi^{1,2,3}, Andrea Pozzer^{1,4}, and Jos Lelieveld^{1,5}

¹ Max Planck Institute for Chemistry, Atmospheric Chemistry Dept., Mainz, 55128, Germany.

² Forschungszentrum Jülich, Inst. for Energy and Climate Research, IEK-8, Jülich, 52425, Germany.

³ National Observatory of Athens, Inst. for Environmental Research and Sustainable Development, Athens, 15236, Greece.

⁴ International Centre for Theoretical Physics, Trieste, 34151, Italy

⁵ The Cyprus Institute, Climate and Atmosphere Research Center Nicosia, 1645, Cyprus.

Correspondence to: Vlassis A. Karydis (v.karydis@fz-juelich.de)

Abstract. The acidity of atmospheric particulate matter regulates its mass, composition and toxicity, and has important consequences for public health, ecosystems and climate. Despite these broad impacts, the global distribution and evolution of aerosol particle acidity are unknown. We used the comprehensive atmospheric multiphase chemistry – climate model EMAC to investigate the main factors that control aerosol particle acidity and uncovered remarkable variability and unexpected trends during the past 50 years in different parts of the world. Aerosol particle acidity decreased strongly over Europe and North America during the past decades while at the same time it increased over Asia. Our simulations revealed that these aerosol particle acidity trends ~~is~~ are strongly related to changes in the phase partitioning of nitric acid, production of sulfate in aqueous aerosols, and the aerosol hygroscopicity. It is remarkable that the aerosol hygroscopicity (κ) has increased in many regions following the aerosol-particle pH. Overall, we find that alkaline compounds, notably ammonium, and to a lesser extent crustal cations, regulate the aerosol-particle pH on a global scale. Given the importance of aerosol particles for the atmospheric energy budget, cloud formation, pollutant deposition and public health, alkaline species hold the key to control strategies for air quality and climate change.

1. Introduction

Aerosol particle acidity is a central property of atmospheric particulates that influence clouds, climate and air quality, including impacts on human health (Raizenne et al., 1996; Lelieveld et al., 2015). It affects the partitioning of semi-volatile acids between the gas and particle phases (Guo et al., 2016; Guo et al., 2017; Guo et al., 2018; Nenes et al., 2020), secondary organic aerosol (SOA) formation (Xu et al., 2015; Marais et al., 2016), the solubility of trace metals in aerosol particles (Oakes et al., 2012), associated with their toxicity (Fang et al., 2017) and nutrient capacity (Jickells et al., 2005), the activation of halogens that act as oxidants (Saiz-Lopez and von Glasow, 2012), the conversion of sulfur dioxide (Seinfeld and Pandis, 2006; Cheng et al.,

2016), the particle hygroscopic growth and lifetime (Metzger et al., 2006;Abdelkader et al., 2015;Karydis et al., 2017), and atmospheric corrosivity (Leygraf et al., 2016). Direct measurement of ~~aerosol~~-particle acidity is difficult and associated with much uncertainty, being dependent on filter sampling and the H⁺ molality in the aqueous extract, which is sensitive to artifacts (Pathak et al., 2004). Therefore, particle pH, a commonly used acidity metric of aqueous aerosols, is typically inferred by proxy techniques (Hennigan et al., 2015;Pye et al., 2020). Two of the most common are the ion balance and the molar ratio methods. These methods do not consider the effects of aerosol water and multiphase interactions with gas phase species as well as the partial dissociation of acids (Hennigan et al., 2015). The simultaneous measurement of gas phase species can improve ~~aerosol~~-particle pH estimates by accounting for the phase partitioning of semi-volatile species (e.g., NH₃, HNO₃). However, the accuracy of this approach relies on the availability of information on these species in both the gas and particle phase, being scant in most cases.

The most reliable estimates of pH are obtained with thermodynamic equilibrium models, although the accuracy can be limited by not accounting for all ionic species. For example, most atmospheric chemistry models do not consider crustal elements (e.g., Ca²⁺, Mg²⁺, K⁺) and Na⁺ in sea salt. These species affect the ion balance by influencing the phase partitioning of nitrate and ammonium, especially in areas where aeolian dust is abundant (Karydis et al., 2016). Here we present 50-year global acidity trends of fine particulate matter (i.e. with a diameter < 2.5 μm) by employing the EMAC chemistry – climate model (Jöckel et al., 2010). The pH calculations are performed online with the ISORROPIA II thermodynamic equilibrium model (Fountoukis and Nenes, 2007).

2. Results and Discussion

2.1 Global variability of aerosol particle acidity

Figure 1 shows the modeled near-surface distribution of fine aerosol particle acidity for the 2010-2015 period. We find predominantly acidic particles over the anthropogenically influenced regions in the northern hemisphere and the tropical biomass burning zones, and mostly alkaline particles over deserts and oceans, especially over the southern oceans. The pH typically ranges from 4.0 to 6.7 (5.3 on average) over the western USA since it is affected by crustal cations from the surrounding deserts. Polluted areas located downwind of crustal sources are of special interest since the pH calculations can be sensitive to the aerosol state assumption (see section 4.3). Over Pasadena, the base case model using the stable state mode estimates a mean pH of 5.9 units, while the sensitivity simulation with only liquid particles results in 2.7 pH units (equal to Guo et al. (2017) estimations by using the metastable assumption; Table A1). Our sensitivity analysis revealed that the aerosol state itself is not affected by the state assumption since both stable and metastable predict the same amount of water in the aerosol. Differences in the calculated pH can be due to the high concentrations of calcium from the Great Basin Desert which results in the precipitation of high amounts of CaSO₄, lowering the particle acidity (but without affecting the water activity since CaSO₄ is insoluble and does not contribute to the MDRH depression). It is worth mentioning that calcium was not

61 included in the Guo et al. (2017) study which helps explain the differences in the observed and simulated aerosol-particle
62 acidity. The simulated particle-phase fraction of nitrate over Pasadena is 40% using the stable state assumption and 32% using
63 the metastable assumption, compared to the observationally derived 51%. Over Europe, the pH ranges from 2.6 to 6.7 (3.9 on
64 average). Observational estimates of aerosol-particle pH from the Po Valley (Squizzato et al., 2013; Masiol et al., 2020) and
65 Cabauw (Guo et al., 2018) support the relatively low acidity of fine aerosols-particles over Europe (Table A1). Model
66 calculations compare well with observational estimates from Cabauw, however, result in higher pH (~1 unit) compared to
67 values from Po Valley (estimated by using the E-AIM model). Over East Asia the average pH is 4.7, ranging from 2.6 to 7.4.
68 Relatively high pH are found over regions where anthropogenic aerosols are mixed with aeolian dust, e.g., from the Gobi
69 Desert, which decrease the acidity (e.g., ~6 pH units over Hohhot, which agrees well with the estimations of Wang et al.
70 (2019a)). The relatively low pH in large parts of Asia is explained by strong SO₂ emissions and associated sulfate, which have
71 increased strongly in the past decades (e.g., over Guangzhou, supported by estimations of Jia et al. (2018)). Estimates of
72 unrealistically high aerosol-particle acidity can result from omitting the gas phase concentrations of semi-volatile ions from
73 the pH calculations (e.g., estimates over Hong Kong (Yao et al., 2007; Xue et al., 2011), Singapore (Behera et al., 2013) and
74 Shanghai (Pathak et al., 2009); Table A1). At the same time, SO₂ emissions have decreased over Europe and USA, and recently
75 in China. However, aerosol particles over the eastern USA have remained acidic, with an average pH of 3.0 until recently,
76 corroborating the findings of Weber et al. (2016) and Lawal et al. (2018) that aerosol particle acidity over this region is less
77 sensitive to SO₂ than to NH₃ emissions.

78 The aerosol-particle pH over polluted northern hemispheric mid-latitudes (e.g., over East Asia) and the northern extratropical
79 oceans exhibits a clear seasonal pattern with lower values during boreal summer and higher ones during winter, driven by the
80 availability of ammonium and by the aerosol water content (Fig. 2). This is evident from both our model calculations and from
81 observational estimates mostly in heavily populated areas such as the Po Valley (Squizzato et al., 2013), Beijing (Tan et al.,
82 2018), and Tianjin (Shi et al., 2017), and to a lesser extent over areas strongly affected by aeolian dust (e.g., Hohhot; Wang et
83 al., 2019b) (Table A1). Over tropical regions, fine particulates have a pH between 3.2 and 7.4, being strongly influenced by
84 pyrogenic potassium, i.e., from widespread biomass burning (Metzger et al., 2006), and a high aerosol water content.
85 Observational estimates from Sao Paulo support these high pH values (Vieira-Filho et al., 2016), albeit with 1 unit bias mainly
86 related to the use of the E-AIM model. Over deserts, aerosol-particles are relatively alkaline, with a pH up to 7.4. Aerosol
87 pParticles in the marine environment tend to be alkaline also, with a pH up to 7.4 over the southern oceans. Observational
88 estimates report highly acidic aerosol-particles over the southern oceans due to the lack of gas phase input for the pH
89 calculations (Dall'Osto et al., 2019). Over the Arctic and the northern Atlantic and Pacific Oceans, aerosol-particle acidity is
90 significantly enhanced by strong sulfur emissions from international shipping and pollution transport from industrialized areas
91 (Fig. 1). The pH over the northern extratropical oceans and the Arctic ranges from 2.0 to 7.0 with an average of about 5.2. The
92 annual cycle of aerosol-particle acidity over these regions is strongly influenced by anthropogenic pollution, being relatively
93 high during boreal summer. Over the Antarctic, aerosol-particle pH ranges from 4.5 to 7.0 and follows a clear seasonal pattern
94 (Fig. 2).

95 2.2 Temporal evolution of aerosol particle acidity

96 Figure 1 and Table 1 present the aerosol particle pH over the period 1970-2020. We investigated the impacts of alkaline species
97 by omitting the emissions of ammonia and mineral cations in two sensitivity simulations.

98 2.2.1 Europe

99 Over Europe, the pH has increased strongly from about 2.8 during the 1970s to 3.9 recently. Especially during the 1990s NH₃
100 emissions over Europe increased significantly by 14%, while at the same time NO_x and SO₂ emissions decreased by 13% and
101 49%, respectively. While this trend has continued in the past decade, pH changes slowed because the sulfate and nitrate
102 decreases have been compensated through volatilization of ammonia from the particles. In addition, the recently increasing
103 cation/anion ratio is accompanied by a reduction of aerosol water, preventing a significant decrease of the aerosol-particle
104 acidity (Fig. S1). Overall, the increase of aerosol particle pH by more than 1 unit during the last 50 years had a significant
105 impact on the gas-particle partitioning of semi-volatile acids, e.g., nitric acid, since their dissociation into ions enhances their
106 solubility (Nah et al., 2018). Here, the fraction of nitrate in the particle phase relative to total nitrate (gas plus particle) has
107 increased from ~70% to 85% (Fig. 3). The increase in aerosol-particle pH has been accompanied by an increase in aerosol
108 kappa hygroscopicity (Fig. 4). After the substantial reduction of SO₂ emissions, sulfate salts (e.g., ammonium sulfate with
109 kappa=0.53) are replaced by more hygroscopic nitrate salts (e.g., ammonium nitrate with kappa=0.67) in the aerosol
110 composition. In addition, the decrease of organic compound emissions during the last 50 years contributed to the increase of
111 the aerosol hygroscopicity. Our sensitivity simulations reveal that aerosol-particle acidity over Europe is highly sensitive to
112 NH₃ emissions. Despite the decline of both SO₂ and NO_x during the past decades, the aerosol-particle would have remained
113 highly acidic (pH ~1) in the absence of NH₃.

114 2.2.2 North America

115 Over North America, aerosol-particle acidity also decreased with SO₂ and NO_x emissions. Nevertheless, these emissions are
116 still relatively strong in the eastern USA (5 times higher than in the western USA) resulting in very acidic aerosol particles,
117 with a pH ranging from 2.2 in 1971 to 3.3 recently (Figs. 1 and S1). Such acidic conditions promote the dissolution of metals
118 (e.g., Fe, Mn, Cu) in ambient particles (Fang et al., 2017). Soluble transition metals in atmospheric aerosols have been linked
119 to adverse health impacts since they generate reactive oxygen species, leading to oxidative stress and increased toxicity of fine
120 particulate matter (Fang et al., 2017; Park et al., 2018). Since the solubility of transition metals increases exponentially below
121 a pH of 3, the decrease of aerosol-particle acidity over the eastern USA reported here suggests that the particles have become
122 substantially less toxic in the past few decades. Similar to Europe, the increasing pH has resulted in a growing aerosol particle
123 nitrate fraction from ~50% during the 1970s to 65% recently (Fig. 3), and to a strong increase of aerosol hygroscopicity by
124 ~0.15 units at the cloud base (Fig. 4). The role of NH₃ is critically important; without it the aerosol-particle pH over the eastern

125 USA would be close to zero. Over the western USA, the aerosol-particle pH is higher (~5), being affected by aeolian dust from
126 the Great Basin Desert, although NH₃ is still the most important alkaline buffer.

127 2.2.3 East and South Asia

128 In Asia, SO₂ and NO_x emissions have increased drastically since 1970. However, the simultaneous increase of NH₃ emissions
129 along with the presence of mineral dust from the surrounding deserts (i.e., Gobi, Taklimakan, Thar) decelerated the increase
130 of aerosol-particle acidity. Over East Asia, the aerosol-particle pH decreased from about 5.3 during the 1970s to 4.5 in 2010.
131 This change in aerosol-particle acidity has affected the predominant pathway of sulfate formation through aerosol aqueous
132 phase chemistry. Under acidic conditions, SO₂ is mainly oxidized by transition metal ions, while at pH > 5 the oxidation by
133 O₃ and NO₂ predominates (Cheng et al., 2016). Therefore, the decrease of pH during the last 50 years, even though being
134 relatively modest, was sufficient to turn-off sulfate production from O₃ oxidation (Fig. 5). At the same time, the increased
135 aerosol-particle acidity hinders the partitioning of nitric acid to the particle phase, reducing the aerosol nitrate fraction from
136 90% to 80% (Fig. 3). Remarkably, the aerosol hygroscopicity has increased from ~0.3 in the 1970s to 0.45 recently (Fig. 4),
137 revealing a reverse development compared to Europe and the USA. Here, the fraction of mineral dust in the aerosol is higher;
138 therefore, the particles gained hygroscopicity by the acquired pollution solutes. Recently, the SO₂ emissions have dropped and
139 the NO_x emission increase has slowed in East Asia, while SO₂ emissions are soaring in South Asia. SO₂ emission trends since
140 2007 have been so drastic that inventories and scenarios tend to overestimate the emitted SO₂. Satellite observations indicate
141 that India has recently overtaken China as the world largest emitter of SO₂ (Li et al., 2017). Following the satellite observations,
142 we implemented the significant SO₂ reduction trends into our model (Fig. S2). Surprisingly, the effect only becomes noticeable
143 over East Asia after 2016, when the aerosol-particle pH started increasing by about 0.3 units, while we do not find any change
144 over South Asia. This corroborates the strong buffering that we found over other regions such as Europe. Fig. 1 shows that
145 NH₃ has been the major buffer, supporting the recent findings of Zheng et al. (2020) that the acid-base pair of NH₄⁺/NH₃
146 provides the largest buffering capacity over East and South Asia. However, we also found that in East Asia and to a lesser
147 extent in South Asia crustal elements, not considered in the study of Zheng et al. (2020), have contributed significantly on
148 maintaining a mean pH of 4.5 – 5 in the past decade (Fig. 1). Calcium is the major crustal component of dust from the Gobi
149 and Taklimakan deserts (Karydis et al., 2016) and unlike other crustal compounds it can react with sulfate ions and form
150 insoluble CaSO₄, which precipitates out of the aerosol aqueous phase. This interaction reduces the aqueous sulfate and thus
151 the aerosol-particle acidity.

152 2.2.4 Tropical forests, Middle East

153 Over tropical forests, aerosol particles are typically not very acidic with pH values >4. Note that organic acids were not
154 included in the aerosol-particle pH calculations, however, their contribution to the total ionic load is small (Andreae et al.,
155 1988;Falkovich et al., 2005), and aerosol-particle acidity can be attributed to inorganic acids. Over the Amazon and Congo
156 basins, the aerosol-particle pH remained around 5 since 1970. The Southeast Asian forest atmosphere is affected by pollution

157 from mainland Asia, and the ~~aerosol~~-particle pH decreased to around 4 recently. This pH drop has enhanced SOA formation
158 from isoprene, since under low-NOx conditions (typical over rainforests) the presence of acidifying sulfate increases the
159 reactive uptake of epoxydiols (Xu et al., 2015;Surratt et al., 2010). Nevertheless, NH₃ emissions provide a remarkably strong
160 buffer over all three tropical regions while mineral dust cations are also important over the Amazon and Congo forests. Further,
161 the Middle East is affected by strong anthropogenic (fossil fuel related) and natural (aeolian dust) aerosol sources. Due to the
162 high abundance of mineral dust, the pH has remained close to 7. Without crustal cations, the pH would drop to about 4. Despite
163 the omnipresence of alkaline species from the surrounding deserts, NH₃ still plays a central role in controlling the acidification
164 of mineral dust aerosols, which can affect their hygroscopic growth and hence their climate forcing (Klingmuller et al.,
165 2019;Klingmüller et al., 2020).

166 2.2.5 Oceans

167 Over the Arctic and northern extra-tropical oceans, ~~aerosol~~-particle acidity is strongly affected by pollution transport from the
168 urban-industrial mid-latitudes. The Arctic ~~aerosol~~-particle pH is highly variable, remaining relatively low up to 1990 (~4.2),
169 after which it increased to about 5.2. Crustal cations are found to play a significant role lowering the ~~aerosol~~-particle acidity.
170 Over the northern extra-tropical oceans, ~~aerosol~~-particle pH has remained relatively constant (~4.8). NH₃ provides an important
171 alkaline buffer, and without it the ~~aerosol~~-particle pH would have been below 3. NH₃ is also proved to be important over the
172 tropical and southern extra-tropical oceans, where a noticeable increase in aerosol particle acidity occurred after June 1991,
173 when the eruption of Mount Pinatubo in the Philippines released ~20 million tons of SO₂ into the stratosphere (McCormick et
174 al., 1995). The impact of Pinatubo sulfate, after returning to the troposphere, on ~~aerosol~~-particle acidity is mostly evident over
175 Antarctica, where the pH dropped by 2 units, as the stratospheric circulation is strongest in the winter hemisphere. Over
176 Antarctica concentrations of dust and especially of NH₃ are very low, and Fig. 1 illustrates that only in this pristine environment
177 the large Pinatubo anomaly could overwhelm the buffering by alkaline species. Except after Pinatubo, the pH has remained
178 nearly constant at 5.8 over Antarctica and about 5.5 in the tropics and 6.8 in the southern extra-tropics.

179 3. Conclusions

180 We find that over Europe and North America the aerosol particle acidity decreased strongly in the past few decades resulting
181 in substantially less toxic and more hygroscopic aerosols. At the same time, the particle acidity over Asia has
182 ~~decreased~~increased, even though the increase of NH₃ emissions and the presence of mineral dust decelerated the change in the
183 ~~aerosol-particle~~ pH. The inevitable decrease of the ~~aerosol~~-particle pH hindered the partitioning of nitric acid into the particulate
184 phase and the sulfate production in the aerosol aqueous phase; however, the aerosol hygroscopicity increased over Asia
185 following a reverse correlation with the particle pH. Overall, the aerosol particle pH is generally well-buffered by alkaline
186 compounds, notably NH₃ and in some areas crustal elements. NH₃ is found to supply remarkable buffering capacity on a global
187 scale, from the polluted continents to the remote oceans. In the absence of NH₃, aerosol particles would be highly (to extremely)

188 acidic in most of the world. Therefore, potential future changes in NH₃ are critically important in this respect. Agriculture is
189 the main NH₃ source and a controlling factor in fine particle concentrations and health impacts in some areas (e.g., Europe)
190 (Pozzer et al., 2017). The control of agricultural ammonia emissions must therefore be accompanied by very strong reductions
191 of SO₂ and NO_x to avoid that aerosol particles become highly acidic with implications for human health (aerosol toxicity),
192 ecosystems (acid deposition and nutrient availability), clouds and climate (aerosol hygroscopicity).

193 **4. Appendix A: Materials and Methods**

194 **4.1 Aerosol-chemistry-climate model**

195 We used the ECHAM5/MESy Atmospheric Chemistry (EMAC) model, which is a numerical chemistry and climate
196 simulation system that describes lower and middle atmosphere processes (Jöckel et al., 2006). EMAC uses the Modular Earth
197 Submodel System (MESSy2) (Jöckel et al., 2010) to link the different sub-models with an atmospheric dynamical core, being
198 an updated version of the 5th generation European Centre - Hamburg general circulation model (ECHAM5) (Roeckner et al.,
199 2006). EMAC has been extensively described and evaluated against in situ observations and satellite retrievals to compute
200 particulate matter concentrations and composition, aerosol optical depth, acid deposition, gas phase mixing ratios, cloud
201 properties, and meteorological parameters (Karydis et al., 2016;Pozzer et al., 2012;Tsimpidi et al., 2016;Karydis et al.,
202 2017;Bacer et al., 2018). The spectral resolution of EMAC used in this study is T63L31, corresponding to a horizontal grid
203 resolution of approximately 1.9°x1.9° and 31 vertical layers extending up to 10 hPa (i.e., 25 km) from the surface. The presented
204 model simulations encompass the 50-year period 1970-2020.

205 EMAC calculates fields of gas phase species online through the Module Efficiently Calculating the Chemistry of the
206 Atmosphere (MECCA) Submodel (Sander et al., 2019). MECCA calculates the concentration of a range of gases, including
207 aerosol precursor species (e.g. SO₂, NH₃, NO_x, DMS, H₂SO₄ and DMSO) and the major oxidant species (e.g. OH, H₂O₂, NO₃,
208 and O₃). Aerosol microphysics are calculated by the Global Modal-aerosol eXtension (GMXe) module (Pringle et al., 2010).
209 The organic aerosol formation and atmospheric evolution are calculated by the ORACLE Submodel (Tsimpidi et al., 2014,
210 2018). The aerosol size distribution is described by seven lognormal modes: four hydrophilic modes that cover the aerosol size
211 spectrum of nucleation, Aitken, accumulation and coarse modes, and three hydrophobic modes that cover the same size range
212 except nucleation. The aerosol composition within each size mode is uniform (internally mixed), however, it varies between
213 modes (externally mixed). Each mode is defined in terms of total number concentration, number mean radius, and geometric
214 standard deviation (Pringle et al., 2010). The removal of gas and aerosol species through wet and dry deposition is calculated
215 within the SCAV (Tost et al., 2006) and DRYDEP (Kerkweg et al., 2006) submodels, respectively. The sedimentation of
216 aerosols is calculated within the SEDI submodel (Kerkweg et al., 2006). The cloud cover, microphysics and precipitation of
217 large scale clouds is calculated by the CLOUD Submodel (Roeckner et al., 2006) which uses a two-moment stratiform
218 microphysical scheme (Lohmann and Ferrachat, 2010), and describes liquid droplet (Karydis et al., 2017) and ice crystal (Bacer

219 et al., 2018) formation by accounting for the aerosol physicochemical properties. The effective hygroscopicity parameter κ is
220 used to describe the influence of chemical composition on the cloud condensation nuclei (CCN) activity of atmospheric
221 aerosols. κ is calculated using the mixing rule of Petters and Kreidenweis (Petters and Kreidenweis, 2007) and the individual
222 κ parameter values for each inorganic salt (Petters and Kreidenweis, 2007; Sullivan et al., 2009). Organic aerosol species are
223 assumed to have a constant hygroscopicity kappa parameter of 0.14 while bulk mineral dust and black carbon are assumed to
224 have zero hygroscopicity.

225 4.2 Emissions

226 The vertically distributed (Pozer et al., 2009) CMIP5 RCP8.5 emission inventory (van Vuuren et al., 2011) is used for the
227 anthropogenic and biomass burning emissions during the years 1970-2020. Direct emissions of aerosol components from
228 biofuel and open biomass burning are considered by using scaling factors applied on the emitted black carbon based on the
229 findings of Akagi et al. (Akagi et al., 2011) (Table S1). Dust emission fluxes and emissions of crustal species (Ca^{2+} , Mg^{2+} , K^+ ,
230 Na^+) are calculated online as described by Klingmuller, et al. (Klingmuller et al., 2018) and based on the chemical composition
231 of the emitted soil particles in every grid cell (Karydis et al., 2016); Table S2. NO_x produced by lightning is calculated online
232 and distributed vertically based on the parameterization of Grewe, et al. (Grewe et al., 2001). The emissions of NO from soils
233 are calculated online based on the algorithm of Yienger and Levy (Yienger and Levy, 1995). The oceanic DMS emissions are
234 calculated online by the AIRSEA Submodel (Pozer et al., 2006). The natural emissions of NH_3 are based on the GEIA
235 database (Bouwman et al., 1997). Emissions of sea spray aerosols (assuming a composition suggested by Seinfeld and Pandis
236 (Seinfeld and Pandis, 2006); Table S1) and volcanic degassing emissions of SO_2 are based on the offline emission data set of
237 AEROCOM (Dentener et al., 2006).

238

239 4.3 Thermodynamic model

240 The inorganic aerosol composition, which is of prime importance for the accurate pH calculation, is computed with the
241 ISORROPIA-II thermodynamic equilibrium model (Fountoukis and Nenes, 2007). ISORROPIA-II calculates the
242 gas/liquid/solid equilibrium partitioning of the K^+ - Ca^{2+} - Mg^{2+} - NH_4^+ - Na^+ - SO_4^{2-} - NO_3^- - Cl^- - H_2O aerosol system and considers the
243 presence of 15 aqueous phase components and 19 salts in the solid phase. ISORROPIA-II solves for the equilibrium state by
244 considering the chemical potential of the species and minimizes the number of equations and iterations required by considering
245 specific compositional “regimes”. The assumption of thermodynamic equilibrium is a good approximation for fine-mode
246 aerosols that rapidly reach equilibrium. However, the equilibrium timescale for large particles is typically larger than the time
247 step of the model (Meng and Seinfeld, 1996) leading to errors in the size distribution of semi-volatile ions like nitrate. Since
248 the current study include reactions of nitric acid with coarse sea-salt and dust aerosol cations, the competition of fine and
249 coarse particles for the available nitric acid can only be accurately represented by taking into account the kinetic limitations

250 during condensation of HNO_3 in the coarse mode aerosols. To account for kinetic limitations by mass transfer and transport
251 between the gas and particle phases, the process of gas/aerosol partitioning is calculated in two stages (Pringle et al., 2010).
252 First, the gaseous species that kinetically condense onto the aerosol phase within the model timestep are calculated assuming
253 diffusion limited condensation (Vignati et al., 2004). Then, ISORROPIA-II re-distributes the mass between the gas and the
254 aerosol phase assuming instant equilibrium between the two phases.

255 ISORROPIA-II is used in the forward mode, in which the total (i.e., gas and aerosol) concentrations are given as input.
256 Reverse mode calculations (i.e. when only the aerosol phase composition is known) should be avoided since they are sensitive
257 to errors and infer bimodal behaviour with highly acidic or highly alkaline particles, depending on whether anions or cations
258 are in excess (Song et al., 2018). While it is often assumed that aerosols are in a metastable state (i.e., composed only of a
259 supersaturated aqueous phase), here we use ISORROPIA-II in the thermodynamically stable state mode where salts are
260 allowed to precipitate once the aqueous phase becomes saturated. For this purpose, we have used the revised ISORROPIA-II
261 model which includes modifications proposed by Song et al. (2018), who resolved coding errors related to pH calculations
262 when the stable state assumption is used. By comparing with the benchmark thermodynamic model E-AIM, Song et al. (2018)
263 found that ISORROPIA-II produces somewhat higher pH (by 0.1-0.7 units, negatively correlated with RH). However, E-AIM
264 model versions either lack crustal cations from the ambient mixture of components (e.g. version II) (Clegg et al., 1998), or
265 only include Na^+ with the restriction that it should be used when $\text{RH} > 60\%$ (e.g. version IV) (Friese and Ebel, 2010). Song et
266 al. (2018) applied the revised ISORROPIA-II during winter haze events in eastern China and found that the assumed particle
267 phase state, either stable or metastable, does not significantly impact the pH predictions.

268 We performed a sensitivity simulation with only liquid particles (i.e., metastable), which revealed that the assumed particle
269 phase state does not significantly impact the pH calculations over oceans and polluted regions (e.g., Europe), however, the
270 metastable assumption produces more acidic particles (up to 2 units of pH) in regions affected by high concentrations of crustal
271 cations and consistently low RH values (Fig. S3). Fountoukis et al. (2007) have shown that the metastable solution predicts
272 significant amounts of water below the mutual deliquescence relative humidity (MDRH, where all salts are simultaneously
273 saturated with respect to all components). Further, the generally high calcium concentrations downwind of deserts results in
274 increasing pH values due to the precipitation of insoluble salts such as the CaSO_4 . The metastable state assumption fails to
275 reproduce this since it treats only the ions in the aqueous phase. In general, high amounts of crustal species can significantly
276 increase the ~~aerosol~~-particle pH which is consistent with the presence of excess carbonate in the particle phase (Meng et al.,
277 1995). It is worth mentioning that the stable state solution algorithm of ISORROPIA II starts with assuming a dry aerosol, and
278 based on the ambient RH dissolves each of the salts depending on their DRH. However, in the ambient atmosphere, when the
279 RH over a wet particle is decreasing, it may not crystallize below the MDRH but instead remain in a metastable state affecting
280 the uptake of water by the particle and thus the pH. This could be the case in some locations with high diurnal variations of
281 RH. Our sensitivity calculations show that, overall, the stable state assumption produces an about 0.5 units higher global
282 average pH than the metastable assumption. Karydis et al. (2016) have shown that while the aerosol state assumption has a
283 marginal effect on the calculated nitrate aerosol tropospheric burden (2% change), it can be important over and downwind of

284 deserts at very low RHs where nitrate is reduced by up to 60% by using the metastable assumption. This is in accord with the
285 findings of Ansari and Pandis (2000) who suggested that the stable state results in higher concentrations of aerosol nitrate
286 when the RH is low (<35 %) and/or sulfate to nitrate molar ratios are low (<0.25).

287 4.4 pH calculations

288 The pH is defined as the negative decimal logarithm of the hydrogen ion activity ($a_{H^+} = \gamma x_{H^+}$) in a solution:

$$289 \quad pH = -\log_{10}(\gamma x_{H^+}) \quad (A1)$$

290 where x_{H^+} is the molality of hydrogen ions in the solution and γ is the ion activity coefficient of hydrogen. Assuming that γ
291 is unity, the aerosol particle pH can be calculated by using the hydrogen ion concentration in the aqueous particle phase
292 calculated by ISORROPIA-II (in mole m^{-3}) and the aerosol water content calculated by GMXe (in mole Kg^{-1}). GMXe assumes
293 that particle modes are internally mixed and takes into account the contribution of both inorganic and organic (based on the
294 organic hygroscopicity parameter, kappa=0.14 (Tsimpidi et al., 2014)) species to aerosol water.

295 The aerosol particle pH is calculated online at each timestep, and output stored every five hours based on instantaneous
296 concentrations of fine aerosol water and hydrogen ions. The average pH values shown in the manuscript are based on the
297 calculated instantaneous mean pH values. According to the Jensen's inequality (Jensen, 1906), the average of the instantaneous
298 pH values is less than or equal to the pH calculated based on the average of the water and hydrogen ion instantaneous values.
299 We estimate that the average pH calculated based on 5-hourly instantaneous values is approximately 1-3 (~2 globally averaged)
300 units higher than the pH calculated based on the average water and hydrogen ion concentrations. By including online gas-
301 particle partitioning calculations of the NH_3/HNO_3 system in polluted air, as applied here, we find that the aerosol-particle pH
302 is higher by approximately one unit (Guo et al., 2015). Hence by neglecting these aspects the aerosol-particle pH would be
303 low-biased by about 3 units.

304

305 4.5 Comparison against pH estimations from field derived $PM_{2.5}$ compositional data

306 The pH calculated here is compared against pH estimations from field derived $PM_{2.5}$ compositional data around the world
307 compiled by Pye et al. (2020) (Table A1). pH data derived from other particle sizes (e.g., PM_{10}) has been omitted since aerosol
308 particle acidity can vary significantly with size (Zakoura et al., 2020). It should be emphasized that the comparison presented
309 in Table A1 aims to corroborate the spatial variability of pH found in this study and not to evaluate the model calculations.
310 Since direct measurements of aerosol-particle acidity are not available, the observation-based aerosol-particle pH is estimated
311 by employing thermodynamic equilibrium models (e.g., ISORROPIA) and making assumptions that can significantly affect
312 the results, especially when the data are averaged over extended periods, while RH conditions during data collection are not
313 always accounted for, e.g. in studies based on filter sampling. The calculation of aerosol particle acidity on a global scale

314 requires the advanced treatment of atmospheric aerosol chemical complexity, representing the real atmosphere, and beyond
315 the conventional methods used by chemistry-climate models (CCM). The atmospheric chemistry model system EMAC is an
316 ideal tool for this purpose since it is one of the most comprehensive CCM containing advanced descriptions of the aerosol
317 thermodynamics (including e.g. dust-pollution interactions) and organic aerosol formation and atmospheric aging (affecting
318 the aerosol water). Our model calculations for aerosol particle acidity are based on some processes/factors that are not included
319 explicitly, usually neglected by model calculations used to constrain the ~~aerosol~~-particle acidity from observations. Sources of
320 discrepancy between the pH calculations can be the following:

- 321 • The stable/metastable assumption does not affect the pH most of the time, however, in some cases with low RHs and the
322 presence of crustal cations, the metastable assumption results in lower pHs (see section 4.3).
- 323 • Crustal species from deserts and Na^+ from sea salt can elevate the pH significantly in some locations, however, these are
324 often neglected in observations.
- 325 • The organic aerosols (which are treated comprehensively by our model using the module ORACLE and the volatility
326 basis set framework (Tsimpidi et al., 2014)) can contribute significantly to the aerosol water, and thus increase the ~~aerosol~~
327 particle pH. This contribution is not considered by many observational studies.
- 328 • Including gas phase species (e.g., NH_3 , HNO_3) in the pH calculations is important. Using only the aerosol-phase as input
329 (i.e., reverse mode) the inferred pH exhibits bimodal behaviour with very acidic or alkaline values depending on whether
330 anions or cations are in excess (Hennigan et al., 2015). Even if the forward mode is used (without gas phase input), the
331 calculated ~~aerosol~~-particle pH is biased low (approximately 1 pH unit) due to the repartition of semi-volatile anions (i.e.,
332 NH_3) to the gas phase to establish equilibrium (Guo et al., 2015).
- 333 • Another important aspect, not explicitly mentioned in many studies, relates to the methods used to derive the campaign-
334 average (or for 3D models the simulated average) pH. In our model the ~~aerosol~~-particle pH is calculated online (2-minute
335 time resolution), while output is stored every five hours based on instantaneous concentrations of fine particle H_2O and
336 H^+ . This mimics 5-hourly aerosol sampling. Then, the average pH values are calculated from the instantaneous mean pH
337 values (see section 4.4). Often models use average values (and not instantaneous) as output, or field-derived pH
338 calculations use average observed H_2O and H^+ values, which can result in important underestimation (by ~ 1 -3 units) of
339 the ~~aerosol~~-particle pH (Jensen, 1906).
- 340 • Some unrealistically high pH values in a few past studies resulted from coding errors in the stable state assumption of the
341 ISORROPIA II model, which have been corrected in our study following the recommendation of Song et al. (2018).
- 342 • The type of thermodynamic model used is also important. Song et al. (2018) found that ISORROPIA-II produces
343 somewhat higher pH (by 0.1-0.7 units, negatively correlated with RH) compared to the thermodynamic model E-AIM,
344 which is used to observationally-constrain pH in some studies.
- 345 • Measurements of $\text{PM}_{2.5}$ nitrate are not always reliable because of artifacts associated with the volatility of ammonium
346 nitrate (Schaap et al., 2004). Ammonium and nitrate can partially evaporate from Teflon filters at temperatures between

347 15 to 20 °C and can evaporate completely at temperatures above. The evaporation from quartz filters is also significant
348 at temperatures higher than 20 °C. This systematic underestimation of ammonium nitrate can affect the observed chemical
349 composition of the aerosol and thus the pH calculations.

350 • The comparison between global model output and observations at specific locations. This also concerns the aerosol
351 concentrations but is especially important for the aerosol particle acidity. Apart from the size of the model grid cells (i.e.,
352 ~ 1.9°x1.9°), the altitude is also important. The first vertical layer of EMAC is approximately 67m in height. On the other
353 hand, ground observations are typically collected in a height up to 3 m. While the aerosol particles within size modes
354 simulated in our model are well-mixed, perhaps this is not the case for the aerosol particles observed at the surface and
355 potentially close to sources, and thus the aerosol-particle acidity may be higher (e.g., due to the higher contribution from
356 local primary sources like SO₄²⁻, lower water amounts in the aerosol, or lower concentrations of semi-volatile cations like
357 NH₄⁺)
358

359 4.6 Partitioning of nitric acid between the gas and aerosol phases

360 The impact of pH on the fraction of nitrate in the particle phase relative to total nitrate (gas plus particle), i.e., $\epsilon(\text{NO}_3^-)$, during
361 the 50 years of simulation in specific regions is calculated as follows (Nah et al., 2018):

$$362 \quad \epsilon(\text{NO}_3^-) = \frac{H_{\text{HNO}_3}^* WRT(0.987 \times 10^{-14})}{\gamma_{\text{NO}_3^-} \gamma_H + 10^{-\text{pH}} + H_{\text{HNO}_3}^* WRT(0.987 \times 10^{-14})} \quad (A2)$$

363 Where $H_{\text{HNO}_3}^*$ is the combined molality-based equilibrium constant of HNO₃ dissolution and deprotonation, γ 's represent the
364 activity coefficients, W is the aerosol water, R is the gas constant, and T is the ambient temperature. Eq. A2 is equivalent with
365 the instantaneous calculations of ISOROPIA II within EMAC. However, the model output is produced after considering all
366 processes in the model and is not calculated at every timestep. Therefore, the use of Eq. 2 can provide a clearer picture of the
367 impact of pH on HNO₃ gas/particle partitioning since the model output (e.g., gas-phase HNO₃ and nitrate in 4 size modes) is
368 subject to uncertainties related to other processes (e.g., deposition, coagulation, transport, etc.).

369 4.7 Sulfate formation in aqueous aerosols

370 The sulfate production rate on aqueous particles from the heterogeneous oxidation of S(IV) with the dissolved O₃ is given by

$$371 \quad R_o = k [O_3] \quad (A3)$$

372 . The first-order uptake rate, k , from monodisperse aerosols with radius r_a and total aerosol surface A , is calculated following
373 Jacob (Jacob, 2000):

$$374 \quad k = \left(\frac{r_a}{D_g} + \frac{4}{v\gamma} \right)^{-1} A \quad (A4)$$

376 where v is the mean molecular speed of O_3 and D_g is its gas-phase molecular diffusion coefficient calculated as follows:

$$377 \quad D_g = \frac{9.45 \times 10^{17} \times \sqrt{T \left(3.47 \times 10^{-2} + \frac{1}{M} \right)}}{\rho_{air}} \quad (A5)$$

378 where T is the ambient air temperature, ρ_{air} is the air density, and M the molar mass of O_3 . γ is the reaction probability calculated
379 following Jacob (Jacob, 2000) and Shao et al. (Shao et al., 2019).

$$380 \quad \gamma = \left(\frac{1}{\alpha} + \frac{v}{4HRT} \frac{1}{D_a K f_r} \right) \quad (A6)$$

381 where α is the mass accommodation coefficient, D_a is the aqueous-phase molecular diffusion coefficient of O_3 , H is the
382 effective Henry's law constant of O_3 (Sander, 2015), R is the ideal gas constant, f_r is the reacto-diffusive correction term (Shao
383 et al., 2019), and K is the pseudo-first order reaction rate constant between $S(IV)$ and O_3 in the aqueous phase (Seinfeld and
384 Pandis, 2006).

385

386 5. References

- 387 Abdelkader, M., Metzger, S., Mamouri, R. E., Astitha, M., Barrie, L., Levin, Z., and Lelieveld, J.: Dust-air pollution dynamics
388 over the eastern Mediterranean, *Atmospheric Chemistry and Physics*, 15, 9173-9189, 10.5194/acp-15-9173-2015, 2015.
- 389 Akagi, S. K., Yokelson, R. J., Wiedinmyer, C., Alvarado, M. J., Reid, J. S., Karl, T., Crounse, J. D., and Wennberg, P. O.:
390 Emission factors for open and domestic biomass burning for use in atmospheric models, *Atmospheric Chemistry and*
391 *Physics*, 11, 4039-4072, 10.5194/acp-11-4039-2011, 2011.
- 392 Andreae, M. O., Talbot, R. W., Andreae, T. W., and Harriss, R. C.: Formic and acetic acid over the central Amazon region,
393 Brazil. 1. dry season, *Journal of Geophysical Research-Atmospheres*, 93, 1616-1624, 10.1029/JD093iD02p01616, 1988.
- 394 Ansari, A. S., and Pandis, S. N.: The effect of metastable equilibrium states on the partitioning of nitrate between the gas and
395 aerosol phases, *Atmospheric Environment*, 34, 157-168, 10.1016/s1352-2310(99)00242-3, 2000.
- 396 Bacer, S., Sullivan, S. C., Karydis, V. A., Barahona, D., Kramer, M., Nenes, A., Tost, H., Tsimpidi, A. P., Lelieveld, J., and
397 Pozzer, A.: Implementation of a comprehensive ice crystal formation parameterization for cirrus and mixed-phase clouds
398 in the EMAC model (based on MESSy 2.53), *Geoscientific Model Development*, 11, 4021-4041, 10.5194/gmd-11-4021-
399 2018, 2018.
- 400 Behera, S. N., Betha, R., Liu, P., and Balasubramanian, R.: A study of diurnal variations of PM2.5 acidity and related chemical
401 species using a new thermodynamic equilibrium model, *Science of The Total Environment*, 452-453, 286-295,
402 <https://doi.org/10.1016/j.scitotenv.2013.02.062>, 2013.
- 403 Bouwman, A. F., Lee, D. S., Asman, W. A. H., Dentener, F. J., VanderHoek, K. W., and Olivier, J. G. J.: A global high-
404 resolution emission inventory for ammonia, *Global Biogeochemical Cycles*, 11, 561-587, 10.1029/97gb02266, 1997.
- 405 Cheng, Y. F., Zheng, G. J., Wei, C., Mu, Q., Zheng, B., Wang, Z. B., Gao, M., Zhang, Q., He, K. B., Carmichael, G., Poschl,
406 U., and Su, H.: Reactive nitrogen chemistry in aerosol water as a source of sulfate during haze events in China, *Science*
407 *Advances*, 2, 10.1126/sciadv.1601530, 2016.
- 408 Clegg, S. L., Brimblecombe, P., and Wexler, A. S.: Thermodynamic model of the system $H^+-NH_4^+-Na^+-SO_4^{2-}-NB_3^- -Cl^-$ -
409 H_2O at 298.15 K, *J. Phys. Chem. A*, 102, 2155-2171, 10.1021/jp973043j, 1998.
- 410 Craig, R. L., Peterson, P. K., Nandy, L., Lei, Z., Hossain, M. A., Camarena, S., Dodson, R. A., Cook, R. D., Dutcher, C. S., and Ault, A. P.:
411 Direct Determination of Aerosol pH: Size-Resolved Measurements of Submicrometer and Supermicrometer Aqueous Particles,
412 *Analytical Chemistry*, 90, 11232-11239, 10.1021/acs.analchem.8b00586, 2018.
- 413 Dall'Osto, M., Airs, R. L., Beale, R., Cree, C., Fitzsimons, M. F., Beddows, D., Harrison, R. M., Ceburnis, D., O'Dowd, C.,
414 Rinaldi, M., Paglione, M., Nenes, A., Decesari, S., and Simó, R.: Simultaneous Detection of Alkylamines in the Surface

Field Code Changed

415 Ocean and Atmosphere of the Antarctic Sympagic Environment, ACS Earth and Space Chemistry, 3, 854-862,
416 10.1021/acsearthspacechem.9b00028, 2019.

417 Dentener, F., Kinne, S., Bond, T., Boucher, O., Cofala, J., Generoso, S., Ginoux, P., Gong, S., Hoelzemann, J. J., Ito, A.,
418 Marelli, L., Penner, J. E., Putaud, J. P., Textor, C., Schulz, M., van der Werf, G. R., and Wilson, J.: Emissions of primary
419 aerosol and precursor gases in the years 2000 and 1750 prescribed data-sets for AeroCom, Atmos. Chem. Phys., 6, 4321-
420 4344, 2006.

421 Ding, J., Zhao, P., Su, J., Dong, Q., Du, X., and Zhang, Y.: Aerosol pH and its driving factors in Beijing, Atmos. Chem. Phys., 19, 7939-
422 7954, 10.5194/acp-19-7939-2019, 2019.

423 Falkovich, A. H., Graber, E. R., Schkolnik, G., Rudich, Y., Maenhaut, W., and Artaxo, P.: Low molecular weight organic
424 acids in aerosol particles from Rondonia, Brazil, during the biomass-burning, transition and wet periods, Atmospheric
425 Chemistry and Physics, 5, 781-797, 10.5194/acp-5-781-2005, 2005.

426 Fang, T., Guo, H. Y., Zeng, L. H., Verma, V., Nenes, A., and Weber, R. J.: Highly Acidic Ambient Particles, Soluble Metals,
427 and Oxidative Potential: A Link between Sulfate and Aerosol Toxicity, Environmental Science & Technology, 51, 2611-
428 2620, 10.1021/acs.est.6b06151, 2017.

429 Fountoukis, C., and Nenes, A.: ISORROPIA II: a computationally efficient thermodynamic equilibrium model for K^+ - Ca^{2+} -
430 Mg^{2+} - NH_4^+ - Na^+ - SO_4^{2-} - NO_3^- - Cl^- - H_2O aerosols, Atmospheric Chemistry and Physics, 7, 4639-4659, 2007.

431 Fridlind, A. M., and Jacobson, M. Z.: A study of gas-aerosol equilibrium and aerosol pH in the remote marine boundary layer during the
432 First Aerosol Characterization Experiment (ACE 1), Journal of Geophysical Research: Atmospheres, 105, 17325-17340,
433 <https://doi.org/10.1029/2000JD900209>, 2000.

434 Friese, E., and Ebel, A.: Temperature Dependent Thermodynamic Model of the System
435 H^+ - NH_4^+ - Na^+ - SO_4^{2-} - NO_3^- - Cl^- - H_2O , The Journal of Physical Chemistry A, 114, 11595-11631, 10.1021/jp101041j,
436 2010.

437 Grewe, V., Brunner, D., Dameris, M., Grenfell, J. L., Hein, R., Shindell, D., and Staehelin, J.: Origin and variability of upper
438 tropospheric nitrogen oxides and ozone at northern mid-latitudes, Atmospheric Environment, 35, 3421-3433,
439 10.1016/s1352-2310(01)00134-0, 2001.

440 Guo, H., Xu, L., Bougiatioti, A., Cerully, K. M., Capps, S. L., Hite, J. R., Carlton, A. G., Lee, S. H., Bergin, M. H., Ng, N. L.,
441 Nenes, A., and Weber, R. J.: Fine-particle water and pH in the southeastern United States, Atmospheric Chemistry and
442 Physics, 15, 5211-5228, 10.5194/acp-15-5211-2015, 2015.

443 Guo, H., Sullivan, A. P., Campuzano-Jost, P., Schroder, J. C., Lopez-Hilfiker, F. D., Dibb, J. E., Jimenez, J. L., Thornton, J.
444 A., Brown, S. S., Nenes, A., and Weber, R. J.: Fine particle pH and the partitioning of nitric acid during winter in the
445 northeastern United States, Journal of Geophysical Research-Atmospheres, 121, 10355-10376, 10.1002/2016jd025311,
446 2016.

447 Guo, H., Otjes, R., Schlag, P., Kiendler-Scharr, A., Nenes, A., and Weber, R. J.: Effectiveness of ammonia reduction on control
448 of fine particle nitrate, Atmospheric Chemistry and Physics, 18, 12241-12256, 10.5194/acp-18-12241-2018, 2018.

449 Guo, H. Y., Liu, J. M., Froyd, K. D., Roberts, J. M., Veres, P. R., Hayes, P. L., Jimenez, J. L., Nenes, A., and Weber, R. J.:
450 Fine particle pH and gas-particle phase partitioning of inorganic species in Pasadena, California, during the 2010 CalNex
451 campaign, Atmospheric Chemistry and Physics, 17, 5703-5719, 10.5194/acp-17-5703-2017, 2017.

452 He, K., Zhao, Q., Ma, Y., Duan, F., Yang, F., Shi, Z., and Chen, G.: Spatial and seasonal variability of $PM_{2.5}$ acidity at two
453 Chinese megacities: insights into the formation of secondary inorganic aerosols, Atmos. Chem. Phys., 12, 1377-1395, 10.5194/acp-12-
454 1377-2012, 2012.

455 He, P., Alexander, B., Geng, L., Chi, X., Fan, S., Zhan, H., Kang, H., Zheng, G., Cheng, Y., Su, H., Liu, C., and Xie, Z.: Isotopic constraints
456 on heterogeneous sulfate production in Beijing haze, Atmos. Chem. Phys., 18, 5515-5528, 10.5194/acp-18-5515-2018, 2018.

457 Hennigan, C. J., Izumi, J., Sullivan, A. P., Weber, R. J., and Nenes, A.: A critical evaluation of proxy methods used to estimate
458 the acidity of atmospheric particles, Atmospheric Chemistry and Physics, 15, 2775-2790, 10.5194/acp-15-2775-2015,
459 2015.

460 Jacob, D. J.: Heterogeneous chemistry and tropospheric ozone, Atmospheric Environment, 34, 2131-2159, 10.1016/s1352-
461 2310(99)00462-8, 2000.

462 Jensen, J.: On the convex functions and inequalities between mean values, Acta Mathematica, 30, 175-193,
463 10.1007/bf02418571, 1906.

Field Code Changed

464 Jia, S., Wang, X., Zhang, Q., Sarkar, S., Wu, L., Huang, M., Zhang, J., and Yang, L.: Technical note: Comparison and
465 interconversion of pH based on different standard states for aerosol acidity characterization, *Atmos. Chem. Phys.*, 18,
466 11125-11133, 10.5194/acp-18-11125-2018, 2018.

467 Jickells, T. D., An, Z. S., Andersen, K. K., Baker, A. R., Bergametti, G., Brooks, N., Cao, J. J., Boyd, P. W., Duce, R. A.,
468 Hunter, K. A., Kawahata, H., Kubilay, N., laRoche, J., Liss, P. S., Mahowald, N., Prospero, J. M., Ridgwell, A. J., Tegen,
469 I., and Torres, R.: Global iron connections between desert dust, ocean biogeochemistry, and climate, *Science*, 308, 67-71,
470 10.1126/science.1105959, 2005.

471 Jöckel, P., Tost, H., Pozzer, A., Bruehl, C., Buchholz, J., Ganzeveld, L., Hoor, P., Kerkweg, A., Lawrence, M. G., Sander, R.,
472 Steil, B., Stiller, G., Tanarhte, M., Taraborrelli, D., Van Aardenne, J., and Lelieveld, J.: The atmospheric chemistry general
473 circulation model ECHAM5/MESSy1: consistent simulation of ozone from the surface to the mesosphere, *Atmos. Chem.*
474 *Phys.*, 6, 5067-5104, 2006.

475 Jöckel, P., Kerkweg, A., Pozzer, A., Sander, R., Tost, H., Riede, H., Baumgaertner, A., Gromov, S., and Kern, B.: Development
476 cycle 2 of the Modular Earth Submodel System (MESSy2), *Geoscientific Model Development*, 3, 717-752, 2010.

477 Karydis, V. A., Tsimpidi, A. P., Pozzer, A., Astitha, M., and Lelieveld, J.: Effects of mineral dust on global atmospheric nitrate
478 concentrations, *Atmos. Chem. Phys.*, 16, 1491-1509, 10.5194/acp-16-1491-2016, 2016.

479 Karydis, V. A., Tsimpidi, A. P., Bacer, S., Pozzer, A., Nenes, A., and Lelieveld, J.: Global impact of mineral dust on cloud
480 droplet number concentration, *Atmospheric Chemistry and Physics*, 17, 5601-5621, 10.5194/acp-17-5601-2017, 2017.

481 Kerkweg, A., Buchholz, J., Ganzeveld, L., Pozzer, A., Tost, H., and Jöckel, P.: Technical Note: An implementation of the dry
482 removal processes DRY DEPosition and SEDimentation in the Modular Earth Submodel System (MESSy), *Atmos. Chem.*
483 *Phys.*, 6, 4617-4632, 2006.

484 Klingmüller, K., Metzger, S., Abdelkader, M., Karydis, V. A., Stenchikov, G. L., Pozzer, A., and Lelieveld, J.: Revised mineral
485 dust emissions in the atmospheric chemistry-climate model EMAC (MESSy 2.52 DU_Astitha1 KKDU2017 patch),
486 *Geoscientific Model Development*, 11, 989-1008, 10.5194/gmd-11-989-2018, 2018.

487 Klingmüller, K., Lelieveld, J., Karydis, V. A., and Stenchikov, G. L.: Direct radiative effect of dust-pollution interactions,
488 *Atmospheric Chemistry and Physics*, 19, 7397-7408, 10.5194/acp-19-7397-2019, 2019.

489 Klingmüller, K., Karydis, V. A., Bacer, S., Stenchikov, G. L., and Lelieveld, J.: Weaker cooling by aerosols due to dust-
490 pollution interactions, *Atmos. Chem. Phys. Discuss.*, 2020, 1-19, 10.5194/acp-2020-531, 2020.

491 Lawal, A. S., Guan, X. B., Liu, C., Hennehan, L. R. F., Vasilakos, P., Bhogineni, V., Weber, R. J., Nenes, A., and Russell, A.
492 G.: Linked Response of Aerosol Acidity and Ammonia to SO₂ and NO_x Emissions Reductions in the United States,
493 *Environmental Science & Technology*, 52, 9861-9873, 10.1021/acs.est.8b00711, 2018.

494 Lelieveld, J., Evans, J. S., Fnais, M., Giannadaki, D., and Pozzer, A.: The contribution of outdoor air pollution sources to
495 premature mortality on a global scale, *Nature*, 525, 367-371, 10.1038/nature15371, 2015.

496 Leygraf, C., Wallinder, I. O., Tidblad, J., and Graedel, T.: *Atmospheric Corrosion*, John Wiley & Sons, 2016.

497 Li, C., McLinden, C., Fioletov, V., Krotkov, N., Carn, S., Joiner, J., Streets, D., He, H., Ren, X., Li, Z., and Dickerson, R. R.:
498 India Is Overtaking China as the World's Largest Emitter of Anthropogenic Sulfur Dioxide, *Scientific Reports*, 7, 14304,
499 10.1038/s41598-017-14639-8, 2017.

500 Liu, M., Song, Y., Zhou, T., Xu, Z., Yan, C., Zheng, M., Wu, Z., Hu, M., Wu, Y., and Zhu, T.: Fine particle pH during severe haze episodes
501 in northern China, *Geophysical Research Letters*, 44, 5213-5221, <https://doi.org/10.1002/2017GL073210>, 2017.

502 Lohmann, U., and Ferrachat, S.: Impact of parametric uncertainties on the present-day climate and on the anthropogenic aerosol
503 effect, *Atmos. Chem. Phys.*, 10, 11373-11383, 10.5194/acp-10-11373-2010, 2010.

504 Marais, E. A., Jacob, D. J., Jimenez, J. L., Campuzano-Jost, P., Day, D. A., Hu, W., Krechmer, J., Zhu, L., Kim, P. S., Miller,
505 C. C., Fisher, J. A., Travis, K., Yu, K., Hanisco, T. F., Wolfe, G. M., Arkinson, H. L., Pye, H. O. T., Froyd, K. D., Liao, J.,
506 and McNeill, V. F.: Aqueous-phase mechanism for secondary organic aerosol formation from isoprene: application to the
507 southeast United States and co-benefit of SO₂ emission controls, *Atmospheric Chemistry and Physics*, 16, 1603-1618,
508 10.5194/acp-16-1603-2016, 2016.

509 Masiol, M., Squizzato, S., Formenton, G., Khan, M. B., Hopke, P. K., Nenes, A., Pandis, S. N., Tositti, L., Benetello, F., Visin,
510 F., and Pavoni, B.: Hybrid multiple-site mass closure and source apportionment of PM_{2.5} and aerosol acidity at major
511 cities in the Po Valley, *Science of The Total Environment*, 704, 135287, <https://doi.org/10.1016/j.scitotenv.2019.135287>,
512 2020.

513 McCormick, M. P., Thomason, L. W., and Trepte, C. R.: ATMOSPHERIC EFFECTS OF THE MT-PINATUBO ERUPTION,
514 *Nature*, 373, 399-404, 10.1038/373399a0, 1995.

Field Code Changed

Field Code Changed

515 Meng, Z. Y., Seinfeld, J. H., Saxena, P., and Kim, Y. P.: Atmospheric gas-aerosol equilibrium .4. Thermodynamics of
516 carbonates, *Aerosol Science and Technology*, 23, 131-154, 1995.

517 Meng, Z. Y., and Seinfeld, J. H.: Time scales to achieve atmospheric gas-aerosol equilibrium for volatile species, *Atmospheric*
518 *Environment*, 30, 2889-2900, 10.1016/1352-2310(95)00493-9, 1996.

519 Metzger, S., Mihalopoulos, N., and Lelieveld, J.: Importance of mineral cations and organics in gas-aerosol partitioning of
520 reactive nitrogen compounds: case study based on MINOS results, *Atmospheric Chemistry and Physics*, 6, 2549-2567,
521 10.5194/acp-6-2549-2006, 2006.

522 Murphy, J. G., Gregoire, P. K., Tevlin, A. G., Wentworth, G. R., Ellis, R. A., Markovic, M. Z., and VandenBoer, T. C.: Observational
523 constraints on particle acidity using measurements and modelling of particles and gases, *Faraday Discussions*, 200, 379-395,
524 10.1039/C7FD00086C, 2017.

525 Nah, T., Guo, H., Sullivan, A. P., Chen, Y., Tanner, D. J., Nenes, A., Russell, A., Ng, N. L., Huey, L. G., and Weber, R. J.:
526 Characterization of aerosol composition, aerosol acidity, and organic acid partitioning at an agriculturally intensive rural
527 southeastern US site, *Atmos. Chem. Phys.*, 18, 11471-11491, 10.5194/acp-18-11471-2018, 2018.

528 Nenes, A., Pandis, S. N., Weber, R. J., and Russell, A.: Aerosol pH and liquid water content determine when particulate matter
529 is sensitive to ammonia and nitrate availability, *Atmospheric Chemistry and Physics*, 20, 3249-3258, 10.5194/acp-20-3249-
530 2020, 2020.

531 Oakes, M., Ingall, E. D., Lai, B., Shafer, M. M., Hays, M. D., Liu, Z. G., Russell, A. G., and Weber, R. J.: Iron Solubility
532 Related to Particle Sulfur Content in Source Emission and Ambient Fine Particles, *Environmental Science & Technology*,
533 46, 6637-6644, 10.1021/es300701c, 2012.

534 Park, M., Joo, H. S., Lee, K., Jang, M., Kim, S. D., Kim, I., Borlaza, L. J. S., Lim, H., Shin, H., Chung, K. H., Choi, Y.-H.,
535 Park, S. G., Bae, M.-S., Lee, J., Song, H., and Park, K.: Differential toxicities of fine particulate matters from various
536 sources, *Scientific Reports*, 8, 17007, 10.1038/s41598-018-35398-0, 2018.

537 Pathak, R. K., Yao, X. H., and Chan, C. K.: Sampling artifacts of acidity and ionic species in PM2.5, *Environmental Science*
538 *& Technology*, 38, 254-259, 10.1021/es0342244, 2004.

539 Pathak, R. K., Wu, W. S., and Wang, T.: Summertime PM2.5 ionic species in four major cities of China: nitrate formation in
540 an ammonia-deficient atmosphere, *Atmos. Chem. Phys.*, 9, 1711-1722, 10.5194/acp-9-1711-2009, 2009.

541 Petters, M. D., and Kreidenweis, S. M.: A single parameter representation of hygroscopic growth and cloud condensation
542 nucleus activity, *Atmospheric Chemistry and Physics*, 7, 1961-1971, 2007.

543 Pozzer, A., Joeckel, P. J., Sander, R., Williams, J., Ganzeveld, L., and Lelieveld, J.: Technical note: the MESSy-submodel
544 AIRSEA calculating the air-sea exchange of chemical species, *Atmos. Chem. Phys.*, 6, 5435-5444, 2006.

545 Pozzer, A., Jockel, P., and Van Aardenne, J.: The influence of the vertical distribution of emissions on tropospheric chemistry,
546 *Atmospheric Chemistry and Physics*, 9, 9417-9432, 2009.

547 Pozzer, A., de Meij, A., Pringle, K. J., Tost, H., Doering, U. M., van Aardenne, J., and Lelieveld, J.: Distributions and regional
548 budgets of aerosols and their precursors simulated with the EMAC chemistry-climate model, *Atmos. Chem. Phys.* 12,
549 961-987, 2012.

550 Pozzer, A., Tsimpidi, A. P., Karydis, V. A., de Meij, A., and Lelieveld, J.: Impact of agricultural emission reductions on fine-
551 particulate matter and public health, *Atmospheric Chemistry and Physics*, 17, 12813-12826, 10.5194/acp-17-12813-2017,
552 2017.

553 Pringle, K. J., Tost, H., Message, S., Steil, B., Giannadaki, D., Nenes, A., Fountoukis, C., Stier, P., Vignati, E., and Lelieveld,
554 J.: Description and evaluation of GMXe: a new aerosol submodel for global simulations (v1), *Geoscientific Model*
555 *Development*, 3, 391-412, 2010.

556 Pye, H. O. T., Zuenten, A., Fry, J. L., Isaacman-VanWertz, G., Capps, S. L., Appel, K. W., Foroutan, H., Xu, L., Ng, N. L., and Goldstein, A.
557 H.: Coupling of organic and inorganic aerosol systems and the effect on gas-particle partitioning in the southeastern US, *Atmos. Chem.*
558 *Phys.*, 18, 357-370, 10.5194/acp-18-357-2018, 2018.

559 Pye, H. O. T., Nenes, A., Alexander, B., Ault, A. P., Barth, M. C., Clegg, S. L., Collett, J. L., Fahey, K. M., Hennigan, C. J.,
560 Herrmann, H., Kanakidou, M., Kelly, J. T., Ku, I. T., McNeill, V. F., Riemer, N., Schaefer, T., Shi, G. L., Tilgner, A.,
561 Walker, J. T., Wang, T., Weber, R., Xing, J., Zaveri, R. A., and Zuenten, A.: The acidity of atmospheric particles and clouds,
562 *Atmospheric Chemistry and Physics*, 20, 4809-4888, 10.5194/acp-20-4809-2020, 2020.

563 Raizenne, M., Neas, L. M., Damokosh, A. I., Dockery, D. W., Spengler, J. D., Koutrakis, P., Ware, J. H., and Speizer, F. E.:
564 Health effects of acid aerosols on North American children: Pulmonary function, *Environmental Health Perspectives*, 104,
565 506-514, 10.2307/3432991, 1996.

566 Roeckner, E., Brokopf, R., Esch, M., Giorgetta, M., Hagemann, S., Kornbluh, L., Manzini, E., Schlese, U., and Schulzweida,
567 U.: Sensitivity of simulated climate to horizontal and vertical resolution in the ECHAM5 atmosphere model, *Journal of*
568 *Climate*, 19, 3771-3791, 10.1175/jcli3824.1, 2006.

569 Saiz-Lopez, A., and von Glasow, R.: Reactive halogen chemistry in the troposphere, *Chemical Society Reviews*, 41, 6448-
570 6472, 10.1039/c2cs35208g, 2012.

571 Sander, R.: Compilation of Henry's law constants (version 4.0) for water as solvent, *Atmos. Chem. Phys.*, 15, 4399-4981,
572 10.5194/acp-15-4399-2015, 2015.

573 Sander, R., Baumgaertner, A., Cabrera-Perez, D., Frank, F., Gromov, S., Grooss, J. U., Harder, H., Huijnen, V., Jockel, P.,
574 Karydis, V. A., Niemeyer, K. E., Pozzer, A., Hella, R. B., Schultz, M. G., Taraborrelli, D., and Tauer, S.: The community
575 atmospheric chemistry box model CAABA/MECCA-4.0, *Geoscientific Model Development*, 12, 1365-1385,
576 10.5194/gmd-12-1365-2019, 2019.

577 Schaap, M., van Loon, M., ten Brink, H. M., Dentener, F. J., and Buitjes, P. J. H.: Secondary inorganic aerosol simulations
578 for Europe with special attention to nitrate, *Atmos. Chem. Phys.*, 4, 857-874, 10.5194/acp-4-857-2004, 2004.

579 Seinfeld, J. H., and Pandis, S. N.: *Atmospheric Chemistry and Physics: From Air Pollution to Climate Change*, Second ed.,
580 John Wiley & Sons, Inc., Hoboken, New Jersey, 2006.

581 Shao, J., Chen, Q., Wang, Y., Lu, X., He, P., Sun, Y., Shah, V., Martin, R. V., Philip, S., Song, S., Zhao, Y., Xie, Z., Zhang,
582 L., and Alexander, B.: Heterogeneous sulfate aerosol formation mechanisms during wintertime Chinese haze events: air
583 quality model assessment using observations of sulfate oxygen isotopes in Beijing, *Atmos. Chem. Phys.*, 19, 6107-6123,
584 10.5194/acp-19-6107-2019, 2019.

585 Shi, G., Xu, J., Peng, X., Xiao, Z., Chen, K., Tian, Y., Guan, X., Feng, Y., Yu, H., Nenes, A., and Russell, A. G.: pH of
586 Aerosols in a Polluted Atmosphere: Source Contributions to Highly Acidic Aerosol, *Environmental Science & Technology*,
587 51, 4289-4296, 10.1021/acs.est.6b05736, 2017.

588 Song, S., Gao, M., Xu, W., Shao, J., Shi, G., Wang, S., Wang, Y., Sun, Y., and McElroy, M. B.: Fine-particle pH for Beijing
589 winter haze as inferred from different thermodynamic equilibrium models, *Atmos. Chem. Phys.*, 18, 7423-7438,
590 10.5194/acp-18-7423-2018, 2018.

591 Squizzato, S., Masiol, M., Brunelli, A., Pistollato, S., Tarabotti, E., Rampazzo, G., and Pavoni, B.: Factors determining the
592 formation of secondary inorganic aerosol: a case study in the Po Valley (Italy), *Atmos. Chem. Phys.*, 13, 1927-1939,
593 10.5194/acp-13-1927-2013, 2013.

594 Sullivan, R. C., Moore, M. J. K., Petters, M. D., Kreidenweis, S. M., Roberts, G. C., and Prather, K. A.: Effect of chemical
595 mixing state on the hygroscopicity and cloud nucleation properties of calcium mineral dust particles, *Atmospheric*
596 *Chemistry and Physics*, 9, 3303-3316, 2009.

597 Surratt, J. D., Chan, A. W. H., Eddingsaas, N. C., Chan, M. N., Loza, C. L., Kwan, A. J., Hersey, S. P., Flagan, R. C., Wennberg,
598 P. O., and Seinfeld, J. H.: Reactive intermediates revealed in secondary organic aerosol formation from isoprene,
599 *Proceedings of the National Academy of Sciences of the United States of America*, 107, 6640-6645,
600 10.1073/pnas.0911114107, 2010.

601 Tan, T., Hu, M., Li, M., Guo, Q., Wu, Y., Fang, X., Gu, F., Wang, Y., and Wu, Z.: New insight into PM2.5 pollution patterns
602 in Beijing based on one-year measurement of chemical compositions, *Science of The Total Environment*, 621, 734-743,
603 <https://doi.org/10.1016/j.scitotenv.2017.11.208>, 2018.

604 Tao, Y., and Murphy, J. G.: The sensitivity of PM2.5 acidity to meteorological parameters and chemical composition changes: 10-year
605 records from six Canadian monitoring sites, *Atmos. Chem. Phys.*, 19, 9309-9320, 10.5194/acp-19-9309-2019, 2019.

606 Tost, H., Jockel, P. J., Kerkweg, A., Sander, R., and Lelieveld, J.: Technical note: A new comprehensive SCAVenging
607 submodel for global atmospheric chemistry modelling, *Atmos. Chem. Phys.*, 6, 565-574, 2006.

608 Tsimpidi, A. P., Karydis, V. A., Pozzer, A., Pandis, S. N., and Lelieveld, J.: ORACLE (v1.0): module to simulate the organic
609 aerosol composition and evolution in the atmosphere, *Geoscientific Model Development*, 7, 3153-3172, 10.5194/gmd-7-
610 3153-2014, 2014.

611 Tsimpidi, A. P., Karydis, V. A., Pandis, S. N., and Lelieveld, J.: Global combustion sources of organic aerosols: model
612 comparison with 84 AMS factor-analysis data sets, *Atmos. Chem. Phys.*, 16, 8939-8962, 10.5194/acp-16-8939-2016, 2016.

613 Tsimpidi, A. P., Karydis, V. A., Pozzer, A., Pandis, S. N., and Lelieveld, J.: ORACLE 2-D (v2.0): an efficient module to
614 compute the volatility and oxygen content of organic aerosol with a global chemistry-climate model, *Geoscientific Model*
615 *Development*, 11, 3369-3389, 10.5194/gmd-11-3369-2018, 2018.

Field Code Changed

616 van Vuuren, D. P., Edmonds, J., Kainuma, M., Riahi, K., Thomson, A., Hibbard, K., Hurtt, G. C., Kram, T., Krey, V.,
617 Lamarque, J. F., Masui, T., Meinshausen, M., Nakicenovic, N., Smith, S. J., and Rose, S. K.: The representative
618 concentration pathways: an overview, *Climatic Change*, 109, 5-31, 10.1007/s10584-011-0148-z, 2011.

619 Vieira-Filho, M., Pedrotti, J. J., and Fornaro, A.: Water-soluble ions species of size-resolved aerosols: Implications for the
620 atmospheric acidity in São Paulo megacity, Brazil, *Atmospheric Research*, 181, 281-287,
621 <https://doi.org/10.1016/j.atmosres.2016.07.006>, 2016.

622 Vignati, E., Wilson, J., and Stier, P.: M7: An efficient size-resolved aerosol microphysics module for large-scale aerosol
623 transport models, *J. Geophys. Res.-Atmos.*, 109, doi: 10.1029/2003jd004485, 2004.

624 Wang, H., Ding, J., Xu, J., Wen, J., Han, J., Wang, K., Shi, G., Feng, Y., Ivey, C. E., Wang, Y., Nenes, A., Zhao, Q., and
625 Russell, A. G.: Aerosols in an arid environment: The role of aerosol water content, particulate acidity, precursors, and
626 relative humidity on secondary inorganic aerosols, *Science of The Total Environment*, 646, 564-572,
627 <https://doi.org/10.1016/j.scitotenv.2018.07.321>, 2019a.

628 Wang, G., Zhang, R., Gomez, M. E., Yang, L., Levy Zamora, M., Hu, M., Lin, Y., Peng, J., Guo, S., Meng, J., Li, J., Cheng, C., Hu, T., Ren,
629 Y., Wang, Y., Gao, J., Cao, J., An, Z., Zhou, W., Li, G., Wang, J., Tian, P., Marrero-Ortiz, W., Secrest, J., Du, Z., Zheng, J., Shang, D.,
630 Zeng, L., Shao, M., Wang, W., Huang, Y., Wang, Y., Zhu, Y., Li, Y., Hu, J., Pan, B., Cai, L., Cheng, Y., Ji, Y., Zhang, F., Rosenfeld,
631 D., Liss, P. S., Duce, R. A., Kolb, C. E., and Molina, M. J.: Persistent sulfate formation from London Fog to Chinese haze, *Proc Natl
632 Acad Sci U S A*, 113, 13630-13635, 10.1073/pnas.1616540113, 2016.

633 Wang, Y., Li, W., Gao, W., Liu, Z., Tian, S., Shen, R., Ji, D., Wang, S., Wang, L., Tang, G., Song, T., Cheng, M., Wang, G.,
634 Gong, Z., Hao, J., and Zhang, Y.: Trends in particulate matter and its chemical compositions in China from 2013–2017,
635 *Science China Earth Sciences*, 62, 1857-1871, 10.1007/s11430-018-9373-1, 2019b.

636 Weber, R. J., Guo, H. Y., Russell, A. G., and Nenes, A.: High aerosol acidity despite declining atmospheric sulfate
637 concentrations over the past 15 years, *Nature Geoscience*, 9, 282-285, 10.1038/ngeo2665, 2016.

638 Xu, L., Guo, H. Y., Boyd, C. M., Klein, M., Bougiatioti, A., Cerully, K. M., Hite, J. R., Isaacman-VanWertz, G., Kreisberg,
639 N. M., Knote, C., Olson, K., Koss, A., Goldstein, A. H., Hering, S. V., de Gouw, J., Baumann, K., Lee, S. H., Nenes, A.,
640 Weber, R. J., and Ng, N. L.: Effects of anthropogenic emissions on aerosol formation from isoprene and monoterpenes in
641 the southeastern United States, *Proceedings of the National Academy of Sciences of the United States of America*, 112,
642 37-42, 10.1073/pnas.1417609112, 2015.

643 Xue, J., Lau, A. K. H., and Yu, J. Z.: A study of acidity on PM_{2.5} in Hong Kong using online ionic chemical composition
644 measurements, *Atmospheric Environment*, 45, 7081-7088, <https://doi.org/10.1016/j.atmosenv.2011.09.040>, 2011.

645 Yao, X., Ling, T. Y., Fang, M., and Chan, C. K.: Size dependence of in situ pH in submicron atmospheric particles in Hong
646 Kong, *Atmospheric Environment*, 41, 382-393, <https://doi.org/10.1016/j.atmosenv.2006.07.037>, 2007.

647 Yienger, J. J., and Levy, H.: Empirical-model of global soil-biogenic NO_x emissions, *Journal of Geophysical Research-*
648 *Atmospheres*, 100, 11447-11464, 10.1029/95jd00370, 1995.

649 Zakoura, M., Kakavas, S., Nenes, A., and Pandis, S. N.: Size-resolved aerosol pH over Europe during summer, *Atmos. Chem.
650 Phys. Discuss.*, 2020, 1-24, 10.5194/acp-2019-1146, 2020.

651 Zheng, G., Su, H., Wang, S., Andreae, M. O., Pöschl, U., and Cheng, Y.: Multiphase buffer theory explains contrasts in
652 atmospheric aerosol acidity, *Science*, 369, 1374-1377, 10.1126/science.aba3719, 2020.

Field Code Changed

Field Code Changed

Field Code Changed

Field Code Changed

654

655 **Author contributions:** V.A.K. and J.L. planned the research, V.A.K., A.P.T. and A.P. performed the model calculations,
656 V.A.K., A.P., and J.L. analyzed the results, V.A.K. and J.L. wrote the paper. All authors contributed to the manuscript.;

657 **Competing interests:** Authors declare no competing interests. **Code/Data availability:** Data and related material can be
658 obtained from V.A.K. (v.karydis@fz-juelich.de) upon request. **Acknowledgments:** The authors gratefully acknowledge the
659 computing time granted on the supercomputer GAIA at Max Planck Institute for Chemistry, Mainz, and on the supercomputer
660 JURECA through JARA at Forschungszentrum Jülich. The work of V.A.K. is supported by the European Union via its Horizon
661 2020 project FORCeS (GA 821205).

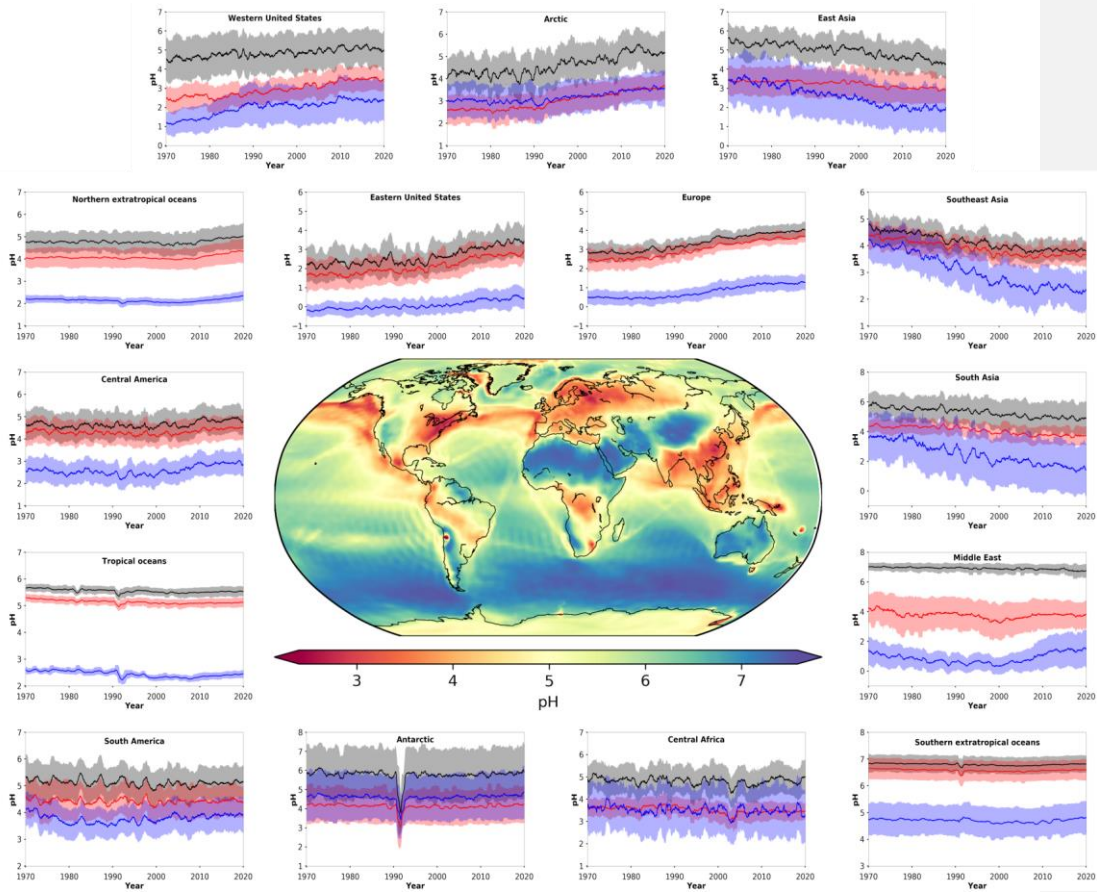
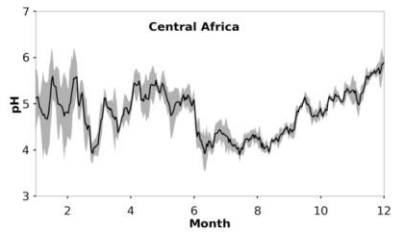
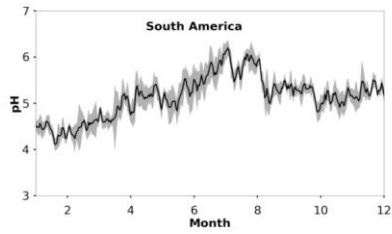
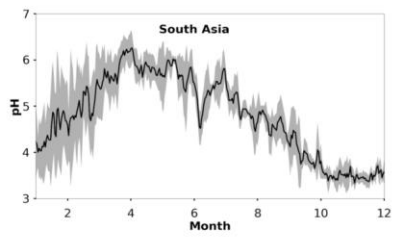
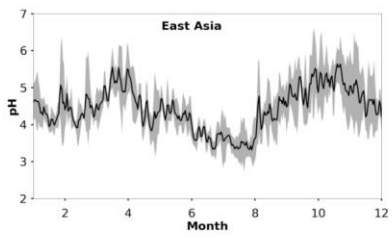
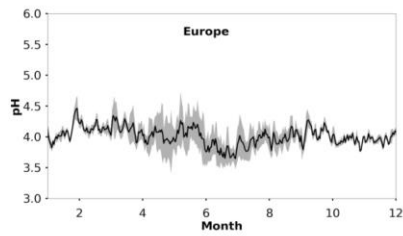
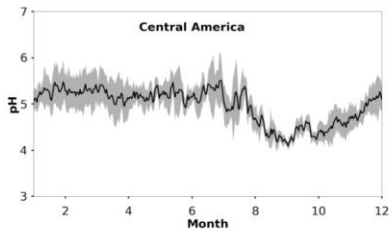
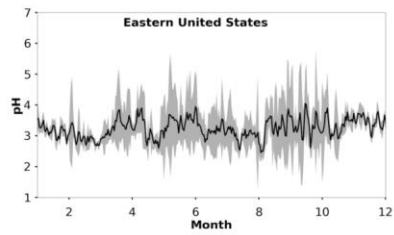
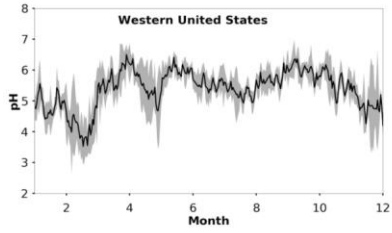


Figure 1: Mean, near-surface fine aerosol particle pH during the period 2010-2015 (central panel). Surrounding panels show the temporal pH evolution during the period 1970-2020 at locations defined in Table 1. Black lines represent the reference simulation. Red and blue lines show the sensitivity simulations in which crustal particle and NH_3 emissions are removed, respectively. Ranges represent the 1σ standard deviation. The anomaly in 1991/2 is related to the Mt Pinatubo eruption.



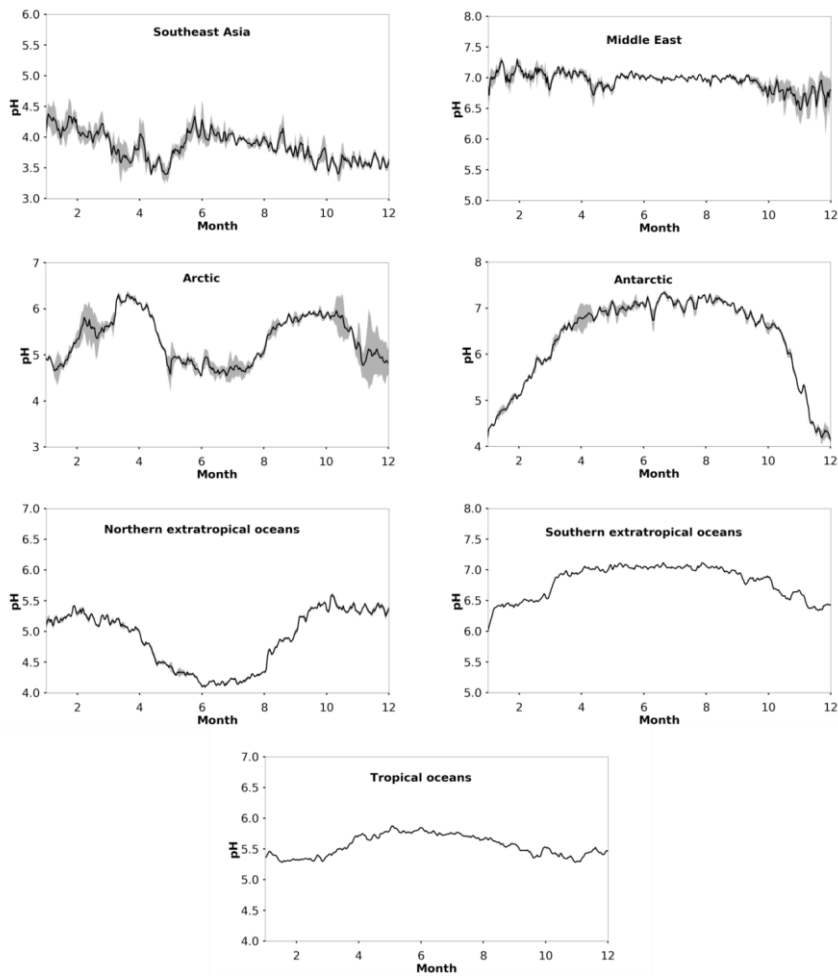


Figure 2: Average seasonal cycle of modelled pH during the period 2010-2015 at locations defined in Table 1. Ranges represent the 1 σ standard deviation.

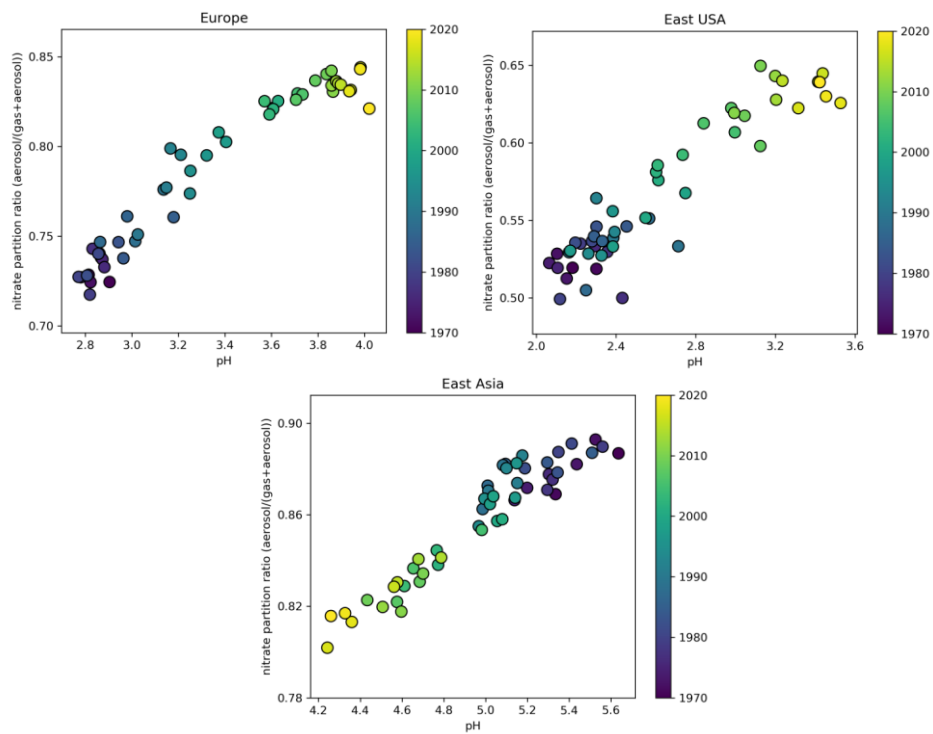


Figure 3: Time evolution of particle phase fraction of total nitrate as a function of pH over Europe (left), the Eastern USA (right) and East Asia (bottom) during the period 1970-2020.

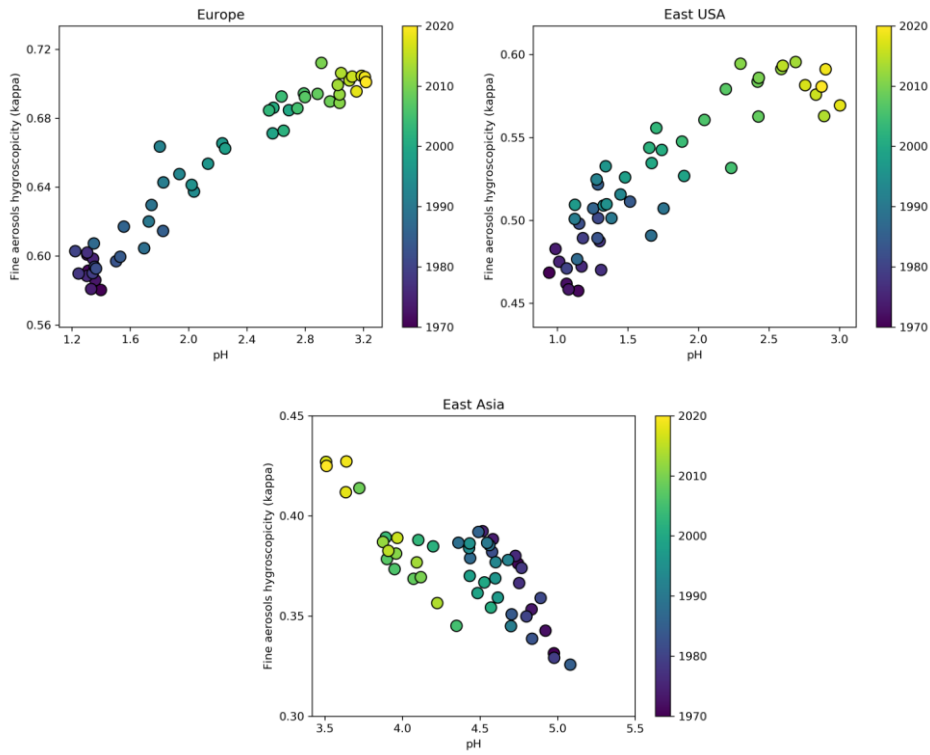


Figure 4: Time evolution of annual average aerosol hygroscopicity (κ) as a function of pH over Europe (left), the Eastern USA (right) and East Asia (bottom) during the period 1970-2020 at the lowest cloud-forming level (940 hPa).

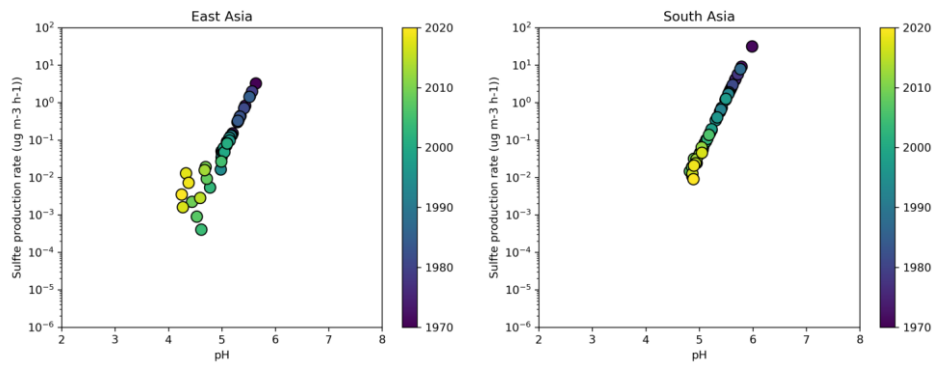


Figure 5: Time evolution of the sulfate production rate on aqueous particles from the SO_2+O_3 multiphase chemistry reaction as a function of aerosol particle pH over East Asia (left) and South Asia (right) during the period 1970-2020.

Table 1: Decadal averages of aerosol particle pH.

Region	Longitude	Latitude	1971-1980	1981-1990	1991-2000	2001-2010	2011-2020
Western USA ¹	90°-70°W	30°-46°N	4.6	4.8	4.8	5.0	5.1
Eastern USA ¹	124°-114°W	30°-52°N	2.2	2.4	2.4	2.9	3.3
Central America ¹	106°-52°W	4°-28°N	4.6	4.6	4.6	4.7	4.9
Europe ¹	12°W-36°E	34°-62°N	2.8	3.0	3.3	3.7	3.9
East Asia ¹	100°-114°E	20°-44°N	5.3	5.2	5.1	4.7	4.5
South Asia ¹	68°-94°E	8°-32°N	5.6	5.5	5.3	5.0	4.9
South America ¹	75°-35°W	30°-0°S	5.2	5.1	5.1	5.1	5.1
Central Africa ¹	10°-40°E	10°S-10°N	4.9	4.8	4.8	4.7	4.9
Southeast Asia ¹	94°-130°E	12°S-20°N	4.5	4.3	4.1	3.9	3.8
Middle East ¹	36°-60°E	12°-34°N	7.0	7.0	6.9	6.9	6.8
Arctic	0°-360°	60°-90°N	4.2	4.2	4.6	4.8	5.2
North extratropics ²	0°-360°	20°-60°N	4.8	4.8	4.7	4.7	4.9
Tropical oceans ²	0°-360°	20°S-20°N	5.6	5.6	5.5	5.5	5.5
South extratropics ²	0°-360°	60°-20°S	6.8	6.8	6.8	6.8	6.8
Antarctic	0°-360°	90°-60°S	5.9	5.9	5.6	5.8	5.8

¹Only values over land are considered for the calculation of pH

²Only values over oceans are considered for the calculation of pH

Table A1: Simulated fine aerosol particle pH compared to observationally-constrained estimates of fine particle acidity compiled by Pye et al. (2020).

Location	Latitude	Longitude	Time period	Simulated mean pH (Stable)	Simulated mean pH (Metastable)	Field derived mean pH	Method used	Reference
Pellston, MI, USA	45.55°N	84.78°W	Jul 2016	3.8	3.1	3.5	pH indicator paper/colorimetric image	Craig et al. (2018)
Ann Arbor, MI, USA	42.28°N	83.74°W	Aug 2016	4.3	3.0	3.5	pH indicator paper/colorimetric image	Craig et al. (2018)
Centreville, AL, USA	32.9°N	87.25°W	Jun 1998 – Aug 2013	6.4	5.7	1.2	ISORROPIA (no NH ₃)	Weber et al. (2016)
Centreville, AL, USA	32.9°N	87.25°W	Jun – Jul 2013	7.0	6.5	1.1	ISORROPIA	Pye et al. (2018)
Egbert, ON, Canada	44.23°N	79.78°W	Jul – Sep 2012	3.9	3.5	2.1	E-AIM Model II	Murphy et al. (2017)
Harrow, ON, Canada	42.03°N	82.89°W	Jun – Jul 2007	4.2	3.0	1.6	E-AIM Model II	Murphy et al. (2017)
Pasadena, CA, USA	34.14°N	118.12°W	Jun 2010	5.9	2.7	2.7	ISORROPIA (metastable)	Guo et al. (2017)
Toronto, Canada	43.66°N	79.40°W	2007-2013	4.0	3.6	2.6	E-AIM I (with gas NH ₃ , HNO ₃)	Tao and Murphy (2019)
Toronto, Canada	43.66°N	79.40°W	2014-2016	4.1	3.7	2.7	E-AIM I (with gas NH ₃ , HNO ₃)	Tao and Murphy (2019)
Ottawa, Canada	45.43°N	75.68°W	2007-2016	4.0	3.9	2.5	E-AIM I (with gas NH ₃ , HNO ₃)	Tao and Murphy (2019)
Simcoe, Canada	42.86°N	80.27°W	2007-2016	4.4	3.7	2.41	E-AIM I (with gas NH ₃ , HNO ₃)	Tao and Murphy (2019)
Montreal, Canada	45.65°N	73.57°W	2007-2016	4.0	3.9	2.4	E-AIM I (with gas NH ₃ , HNO ₃)	Tao and Murphy (2019)
Windsor, Canada	42.29°N	83.07°W	2007-2010	4.4	3.6	2.1	E-AIM I (with gas NH ₃ , HNO ₃)	Tao and Murphy (2019)
Windsor, Canada	42.29°N	83.07°W	2012-2016	4.5	3.7	2.4	E-AIM I (with gas NH ₃ , HNO ₃)	Tao and Murphy (2019)
St. Anicet, Canada	45.12°N	74.29°W	2007-2016	4.0	3.9	2.5	E-AIM I (with gas NH ₃ , HNO ₃)	Tao and Murphy (2019)
Sao Paulo, Brazil	23.55°S	46.63°W	Aug – Sep 2012	6.2	6.1	4.8	E-AIM	Vieira-Filho et al. (2016)
Po Valley, Italy	45.40°N	12.20°E	Mar 2009 – Jan 2010	4.5	3.6	3.1	E-AIM Model IV	Squizzato et al. (2013)

Po Valley, Italy	45.40°N	12.20°E	Spring 2009	4.3	3.7	3.6	E-AIM Model IV	Squizzato et al. (2013)
Po Valley, Italy	45.40°N	12.20°E	Summer 2009	4.8	3.0	2.3	E-AIM Model IV	Squizzato et al. (2013)
Po Valley, Italy	45.40°N	12.20°E	Fall 2009	4.5	3.6	3	E-AIM Model IV	Squizzato et al. (2013)
Po Valley, Italy	45.40°N	12.20°E	Winter 2009-2010	4.4	4.0	3.4	E-AIM Model IV	Squizzato et al. (2013)
Po Valley, Italy	45.40°N	12.20°E	Winter 2012-2013	4.2	4.0	3.9	ISORROPIA (metastable, no NH ₃)	Masiol et al. (2020)
Po Valley, Italy	45.40°N	12.20°E	Spring 2012	4.1	3.1	2.3	ISORROPIA (metastable, no NH ₃)	Masiol et al. (2020)
Cabauw, Netherlands	51.97°N	4.93°E	Jul 2012 – Jun 2013	4.0	3.8	3.7	ISORROPIA	Guo et al. (2018)
Cabauw, Netherlands	51.97°N	4.93°E	Jun – Aug 2013	3.6	3.4	3.3	ISORROPIA	Guo et al. (2018)
Cabauw, Netherlands	51.97°N	4.93°E	Dec – Feb 2012	4.1	4.1	3.9	ISORROPIA	Guo et al. (2018)
Beijing, China	39.99°N	116.30°E	Nov 2015 – Dec 2016	4.9	4.2	4.2	ISORROPIA	Liu et al. (2017)
Guangzhou, China	23.13°N	113.26°E	Jul 2013	2.6	1.9	2.5	E-AIM Model IV	Jia et al. (2018)
Beijing, China	39.97°N	116.37°E	Nov 2014 – Dec 2014	4.5	5.3	4.6	ISORROPIA	Song et al. (2018)
Beijing, China	40.41°N	116.68°E	Oct 2014 – Jan 2015	5.6	4.9	4.7	ISORROPIA (metastable)	He et al. (2018)
Beijing, China	39.99°N	116.31°E	Jan – Dec 2014	4.9	4.0	3.0	ISORROPIA (metastable)	Tan et al. (2018)
Beijing, China	39.99°N	116.31°E	Winter 2014	5.5	4.4	4.1	ISORROPIA (metastable)	Tan et al. (2018)
Beijing, China	39.99°N	116.31°E	Fall 2014	6.0	4.6	3.1	ISORROPIA (metastable)	Tan et al. (2018)
Beijing, China	39.99°N	116.31°E	Spring 2014	5.4	4.5	2.1	ISORROPIA (metastable)	Tan et al. (2018)
Beijing, China	39.99°N	116.31°E	Summer 2014	3.1	2.4	1.8	ISORROPIA (metastable)	Tan et al. (2018)
Tianjin, China	39.11°N	117.16°E	Dec 2014 – Jun 2015	4.4	3.7	4.9	ISORROPIA (metastable)	Shi et al. (2017)
Tianjin, China	39.11°N	117.16°E	Aug 2015	1.4	1.2	3.4	ISORROPIA	Shi et al. (2017)

China							(metastable)	
Beijing, China	39.98°N	116.28°E	Feb 2017	4.7	4.8	4.5	ISORROPIA	Ding et al. (2019)
Beijing, China	39.98°N	116.28°E	Apr - May 2016	5.2	4.7	4.4	ISORROPIA	Ding et al. (2019)
Beijing, China	39.98°N	116.28°E	Jul - Aug 2017	2.2	1.9	3.8	ISORROPIA	Ding et al. (2019)
Beijing, China	39.98°N	116.28°E	Sep - Oct 2017	4.5	3.7	4.3	ISORROPIA	Ding et al. (2019)
Guangzhou, China	23.13°N	113.26°E	Jul - Sep 2013	2.7	2.2	2.4	E-AIM Model III	Jia et al. (2018)
Hohhot, China	40.48°N	111.41°E	Summer 2014	5.5	4.0	5	ISORROPIA (metastable, no NH ₃)	Wang et al., 2019
Hohhot, China	40.48°N	111.41°E	Autumn 2014	6.8	5.3	5.3	ISORROPIA (metastable, no NH ₃)	Wang et al. (2019)
Hohhot, China	40.48°N	111.41°E	Winter 2014	5.8	5.0	5.7	ISORROPIA (metastable, no NH ₃)	Wang et al. (2019)
Hohhot, China	40.48°N	111.41°E	Spring 2015	6.1	5.1	6.1	ISORROPIA (metastable, no NH ₃)	Wang et al. (2019)
Hohhot, China	40.48°N	111.41°E	2014 - 2015	6.2	5.0	5.6	ISORROPIA (metastable, no NH ₃)	Wang et al. (2019)
Beijing, China	40.41°N	116.68°E	Oct 2014 - Jan 2015	5.6	4.9	7.6	ISORROPIA (stable state)	He et al. (2018)
Xi'an, China	34.23°N	108.89°E	Nov - Dec 2012	5.7	4.5	6.7	ISORROPIA	Wang et al. (2016)
Beijing, China	39.99°N	116.30°E	Jan - Feb 2015	5.0	3.8	7.6	ISORROPIA	Wang et al. (2016)
Beijing, China	40.35°N	116.30°E	Jun - Aug 2005	4.2	3.3	0.6	E-AIM Model II (only aerosols)	Pathak et al. (2009)
Shanghai, China	31.45°N	121.10°E	May - Jun 2005	3.5	3.1	0.7	E-AIM Model II (only aerosols)	Pathak et al. (2009)
Lanzhou, China	36.13°N	103.68°E	Jun - Jul 2006	6.8	5.1	0.6	E-AIM Model II (only aerosols)	Pathak et al. (2009)
Beijing, China	40.32°N	116.32°E	Jan 2005 - Apr 2006	5.1	4.1	0.7	E-AIM Model II (only aerosols)	He et al. (2012)
Chongqing, China	29.57°N	106.53°E	Jan 2005 - Apr 2006	3.6	2.7	1.5	E-AIM Model II (only aerosols)	He et al. (2012)
Beijing, China	40°N	116.33°E	Jan 2013	4.6	4.5	5.8	ISORROPIA (forward & reverse, estimated)	Wang et al. (2016)

							NH ₃)	
Singapore	1.3°N	103.78°E	Sep – Nov 2011	3.2	3.0	0.6	E-AIM Model IV	Behera et al. (2013)
Hong Kong	22.34°N	114.26°E	Jul 1997 – May 1998	3.3	3.0	0.3	E-AIM Model II (for RH ≥ 70%)	Yao et al. (2007)
Hong Kong	22.34°N	114.26°E	Nov 1996 – Nov 1997	3.4	2.9	-1	E-AIM Model II (for RH < 70%)	Yao et al. (2007)
Hong Kong	22.34°N	114.26°E	Oct 2008	5.0	3.2	0.6	E-AIM Model III (only aerosols)	Xue et al. (2011)
Hong Kong	22.34°N	114.26°E	Nov 2008	3.7	2.7	-0.5	E-AIM Model III (only aerosols)	Xue et al. (2011)
Hong Kong	22.34°N	114.26°E	Jun - Jul 2009	1.6	2.0	-0.1	E-AIM Model III (only aerosols)	Xue et al. (2011)
Pacific Ocean	47.5°S	147.5°E	Nov - Dec 1995	7.0	6.5	1.0	EQUISOLV	Fridlind and Jacobson (2000)
South Ocean	61°S	45°W	Jan 2015	6.9	6.7	1.4	ISORROPIA (no NH ₃)	Dall'Osto et al. (2019)
South Ocean	64°S	65°W	Jan – Feb 2015	6.9	6.8	3.8	ISORROPIA (no NH ₃)	Dall'Osto et al. (2019)